A Tunable Light Source at 1.6 μm by Difference-Frequency Mixing in Cesium Titanyl Arsenate

by

Bobby Yoke Fung Lai

S.B., Electrical Engineering
S.B., Management Science
Massachusetts Institute of Technology (1992)

Submitted to the
Department of Electrical Engineering and Computer Science
in partial fulfillment of the requirements for the degree of

Master of Science in Electrical Engineering

at the

MASSACHUSETTS INSTITUTE OF TECHNOLOGY

January 1995

Author ....
Department of Electrical Engineering and Computer Science
January 20, 1995

Certified by.... .....
Dr. N. C. Wong
Research Scientist, Research Laboratory of Electronics
Thesis Supervisor

Accepted by..... .....
F. R. Morgenthaler
Chairman, Departmental Committee on Graduate Students

A Tunable Light Source at 1.6 μm by Difference-Frequency Mixing in Cesium Titanyl Arsenate

by

Bobby Yoke Fung Lai

Submitted to the Department of Electrical Engineering and Computer Science
on January 20, 1995, in partial fulfillment of the
requirements for the degree of
Master of Science in Electrical Engineering

Abstract

An optical system is investigated to generate tunable coherent radiation at 1.6 μm by difference-frequency mixing (DFM) in cesium titanyl arsenate ($CsTiOAsO_4$, CTA). The input laser sources are provided by a krypton-ion laser at $\lambda_p = 530.9$ nm and a Ti:sapphire ring laser whose output is tunable from $\lambda_s = 770 - 810$ nm. To increase the generated output power, the CTA crystal is placed inside a cavity, forming a configuration for resonant difference-frequency mixing (RDFM).

To verify the feasibility of the proposed schemes, DFM and RDFM experiments were performed. The generated output by DFM was tunable from 1566.9 nm to 1652.5 nm with output powers in the 1 μW range for a pump power of 156 mW and a signal power of 37 mW. The phase-matching angles for DFM in CTA were also experimentally measured and were compared with those calculated from the Sellmeier equations for CTA. The RDFM experiment was performed for a fixed input signal at $\lambda_s = 790.0$ nm. The maximum generated output idler power at $\lambda_i = 1618.7$ nm was 100 μW for pump and signal powers of 230 mW and 57 mW, respectively.

Thesis Supervisor: Dr. N. C. Wong
Title: Research Scientist, Research Laboratory of Electronics

Acknowledgments

I am very grateful to Dr. Franco Wong for giving me the opportunity to work on a very interesting thesis topic and for his advice on this thesis and other projects during the past two years. It has been a real privilege to work with and learn from someone who has tremendous knowledge and enthusiasm for the field of nonlinear and quantum optics.

I want to thank Kevin Cheng of DuPont for providing the CTA crystal that was used in this thesis.

A special thanks goes to Dicky Lee for his time in helping me perform the experiments and collect the data. He was instrumental in clearing up many questions I had with the theoretical and experimental parts of this thesis. Lastly, I am grateful that he was able to put up with me more than I can put up with myself.

I also want to thank the other members in my group: Reggie Brothers, Steve Patterson, Elliott Mason, Asif Shakeel, Donald Greer, Jeff Bounds, and Phil Nee, for the many stimulating conversations in the lab and offices.

I would like to thank my good friends, Chris Cooke and Ona Wu, for all the fun times we had together and for making life at MIT bearable. I also want to thank Peter Li and Boris Golubovic for their advice on various topics and their friendship. Finally, I want to acknowledge all the numerous friends I have made at MIT for enriching my life.

This thesis is dedicated to my family:
my parents, James Kon Chiang Lai and Toy Ngan Lai;
my brothers, Henry Lai and Keith Lai;
and my sister Diana Lai, for their love and support.

Contents

List of Figures

List of Tables

Chapter 1

Introduction

The laser has made a significant impact in many areas of research by providing a highly coherent source for a wide variety of applications. The numerous types of available lasers can cover a wide wavelength range, but the tuning range of any single laser is, with a few exceptions, very limited. After the laser was invented in the late 1950's, intensive research was performed to develop sources that can provide tunable coherent radiation for the entire optical spectrum. Many applications require sources whose output frequencies can be tuned continuously over a broad spectrum. High-resolution spectroscopy requires a tunable coherent cw radiation that can provide precise wavelength resolution, high power, and good frequency and amplitude stability. A wavelength resolution of better than 1 MHz and an output power greater than 1 μW are desirable for high sensitivity and time-resolved absorption spectroscopy.[8] A wideband highly coherent tunable light source is especially convenient in such areas as quantum optics where measurements in the atomic levels and of fundamental physical constants are required. For precision optical measurements, a coherent optical frequency sweep generator (OFSG) with the frequency coverage from the ultraviolet to the infrared is required as a coherent light source.[27]

A variety of nonlinear frequency conversion techniques can be used to cover a wide frequency range and to generate new frequencies of light. Ironically it was the laser that was responsible for the practical applications of these nonlinear devices. Perhaps the simplest approach to generating tunable radiation is second-order para-

metric generation in nonlinear crystals. Optical parametric generation (OPG) in various nonlinear crystals can provide a practical means to generate coherent tunable radiation from the ultraviolet to the far infrared. The main advantage of OPG sources over conventional tunable sources such as dye lasers is that they offer a much broader tuning bandwidth. In addition, OPG sources can generate radiation in regions that are not conveniently accessible by laser sources and can have very high efficiencies.

Most of the nonlinear second-order interactions can be viewed as three-wave mixing (3WM) processes in which the interaction of two input waves in a second-order nonlinear crystal generates a third wave. If the two input waves at the lower frequencies ω_1 and ω_2 generate a higher frequency wave at $\omega_3 = \omega_1 + \omega_2$, then the process is called sum-frequency mixing (SFM). For the special case of SFM where the two input waves are degenerate ($\omega_1 = \omega_2 = \omega$), we have second-harmonic generation (SHG) since an output at $\omega_3 = 2\omega$ is generated. The other possible interaction in which the two input waves at ω_3 and ω_2 ($\omega_3 > \omega_2$) generate a wave at $\omega_1 = \omega_3 - \omega_2$ is called difference-frequency mixing (DFM). In each of these processes, conversion of energy among the three electromagnetic waves takes place under the condition $\omega_1 + \omega_2 = \omega_3$.

By 1965, all the basic three-wave mixing techniques, including optical parametric amplification and optical parametric oscillation, had been demonstrated using a variety of lasers and nonlinear materials.[7] After the initial progress in the theoretical and experimental studies of three-wave mixing, the development of this kind of tunable source in practical applications was hampered by the limitations of available pump lasers and the lack of nonlinear crystals with desirable properties. Common problems at that time included optical damage to the nonlinear crystal, insufficient crystal nonlinearities, and overly stringent requirements on the laser source. In recent years, interest in three-wave mixing has been renewed because of improved laser sources and improved quality and variety of nonlinear crystals. Innovations in the growth of nonlinear crystals have produced new and better crystals with sufficiently large nonlinearities, high laser damage thresholds, and wide transparency ranges. Some of these nonlinear crystals produced during the past twenty-five years include potassium dihydrogen phosphate (KDP), potassium titanyl phosphate (KTP), beta barium

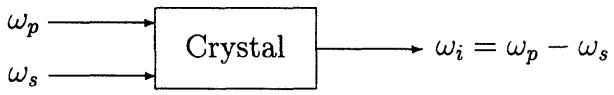

Figure 1-1: The difference-frequency mixing process.

borate (BBO), lithium triborate (LBO), silver thiogallate ($AgGaS_2$), lithium iodate ($LiIO_3$), lithium niobate ($LiNbO_3$), and potassium niobate ($KNbO_3$). As tunable sources by three-wave mixing have improved, they have attracted renewed interest in such applications as combustion diagnostics, process control, remote sensing and environmental monitoring.[13]

1.1 Difference Frequency Mixing

As discussed earlier, difference-frequency mixing (DFM) involves two input waves incident on a second-order nonlinear medium to generate a third wave at the difference frequency of the two input waves. This DFM process is shown in Figure 1-1. Using the conventional terminology for DFM, we will refer to the high frequency input wave as the pump (ω_p), the low frequency input wave as the signal (ω_s), and the output wave as the idler (ω_i). Therefore, the generated idler frequency can be expressed as

$$\omega_i = \omega_p - \omega_s.$$

According to this equation, the idler frequency can be tuned by varying the pump and/or the signal frequency. The common approach is to generate the idler frequency using a tunable laser and a fixed frequency laser as the input sources. For this thesis, a krypton-ion laser provides a fixed wavelength output for the pump and a Ti:sapphire laser is the tunable source for the signal frequency.

Difference-frequency mixing is mainly used to generate coherent radiation in the infrared region. Currently, a wavelength range of great interest in the infrared region is around $1.5 - 1.6$ μm for optical fiber communications. The main sources for this wavelength region are diode lasers. However, the cw output powers and linewidths

of diode lasers are generally unsatisfactory for many applications. In addition, the tunability of any one particular diode laser is limited even though a combination of many diode lasers can be used to cover a large wavelength region. Difference-frequency mixing in nonlinear crystals provides an attractive and simple method to improve these deficiencies of diode lasers.

Generation of tunable infrared radiation by difference-frequency mixing in nonlinear crystals has been widely studied. A large majority of the published article on DFM involves pulsed sources, while cw sources are reported less frequently. A cw pump source offers significantly smaller spectral linewidths than a pulsed source, better frequency stability, and continuous scan possibilities. However, the disadvantage of cw sources is a lower conversion efficiency. For cw DFM, output idler powers are limited to the μW levels for inputs in the 100 mW levels.

Difference-frequency mixing was first demonstrated as a convenient, tunable cw light source for high-resolution infrared spectroscopy by Pine.[23] The spectrometer was realized by mixing the single-frequency outputs from an argon-ion laser and a tunable cw dye laser in a lithium niobate ($LiNbO_3$) crystal to generate a 0.5 μW output from 2.2 to 4.2 μm. Wellegehausen et al. obtained tunable cw infrared radiation from 2.3 to 4.6 μm at about 0.5 μW by noncollinear difference-frequency mixing in lithium iodate ($LiIO_3$).[30] More recently, Heilscher et al. built a cw laser spectrometer based on DFM using Ti:sapphire and dye lasers in silver thiogallate ($AgGaS_2$) to generate outputs from 4.76 to 6.45 μm.[16] Wang and Ohtsu reported DFM in potassium titanyl phosphate (KTP) at 1.6 μm by using two cw single-frequency MQW-DFB diode lasers at 0.78 μm and 1.54 μm to produce an output of 0.3 μW tunable from 1.58-1.62 μm.[27]

This thesis investigates a tunable light source similar to that of Wang and Ohtsu. The main difference is that the 1.6 μm output by difference-frequency mixing is performed in cesium titanyl arsenate ($CsTiOAsO_4$, CTA),[9] using a krypton laser and Ti:sapphire laser as inputs. CTA is a relatively new nonlinear crystal that is isomorphic to KTP and belongs to an orthorhombic system with point group symmetry $mm2$. CTA is a positive biaxial crystal with $n_x < n_y < n_z$, where n is the refrac-

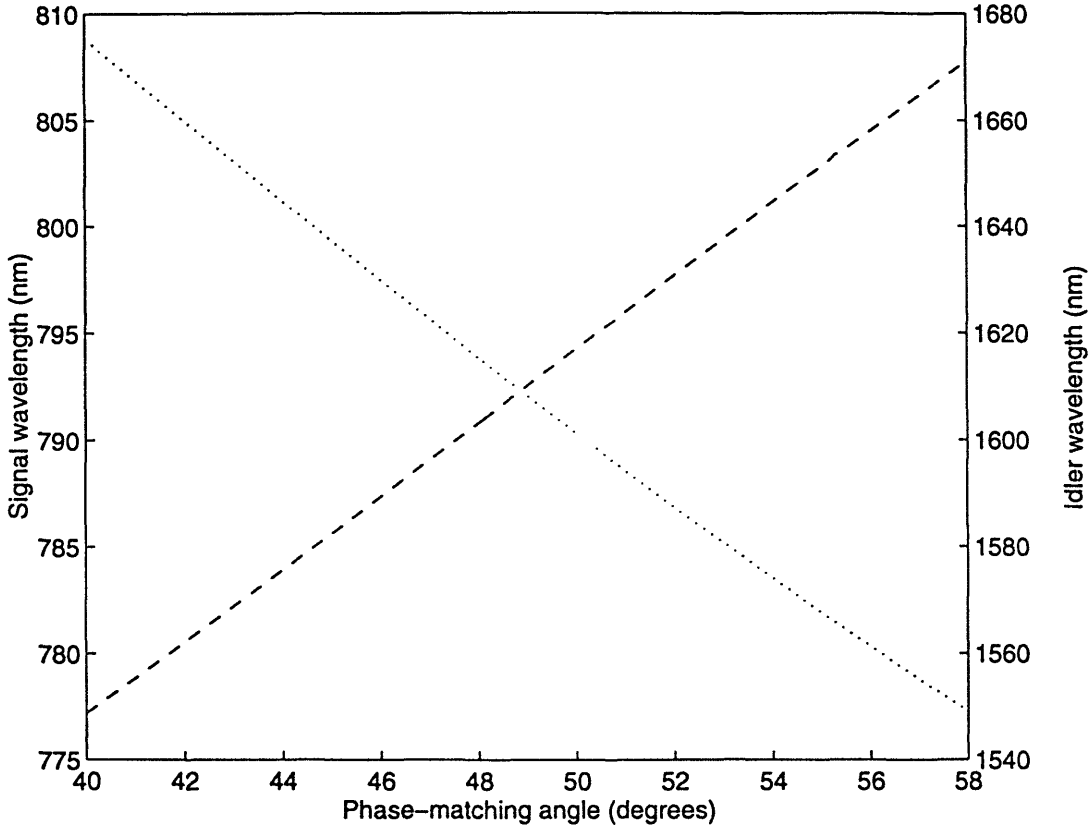

Figure 1-2: Angle tuning characteristics of difference-frequency mixing in CTA for Type II phase-matching in the xy plane ($\theta = 90°$) and a pump wavelength of $\lambda_p = 530.9$ nm. The dashed curve is for the signal wavelength and the dotted curve is for the idler wavelength.

tive index and the subscripts x, y and z refer to the three crystallographic axes. CTA has many desirable optical properties, including large nonlinear coefficients, a high damage threshold, good thermal and chemical stability, and a wide temperature bandwidth for angle phase-matching.[9] Since CTA exhibits a broader infrared transparency range from 0.35 to 5.3 μm and slightly larger nonlinear coefficients than KTP, CTA is potentially better suited than KTP for three-wave mixing at larger wavelengths.

Difference-frequency mixing requires phase-matching among the three interacting waves, limiting the range of idler wavelengths that can be generated. Wavelength tuning of the output idler is then typically achieved by angle or temperature tuning the nonlinear crystal. The Type II phase-matching curve calculated from the Sellmeier equations for CTA is shown in Figure 1-2. According to this graph, to achieve the desired idler output at $\lambda_i = 1.6$ μm for a fixed pump wavelength of $\lambda_p = 530.9$ nm, the required Ti:sapphire laser output wavelength is from $\lambda_s = 780-800$ nm. Furthermore, the range of phase-matching angles is small enough for one CTA crystal to cover a large wavelength region. At the present, no experimental demonstration of difference-frequency mixing in CTA has been reported. In fact, this thesis provides the first demonstration of cw optical parametric generation in CTA.

1.2 Resonant Difference-Frequency Mixing

One way to increase the conversion efficiency of a three-wave mixing process is to place the nonlinear crystal inside an optical cavity. The feedback provided by the cavity enhances the interacting waves that are propagating back and forth inside the resonator. If the increased gain can balance the losses of the cavity, parametric oscillation can occur. For this optical parametric oscillator (OPO), the only input beam is the pump as shown in Figure 1-3. The signal and idler photons generated from parametric fluorescence oscillate forward and backward in the cavity and are amplified each time they propagate through the crystal. Therefore, tunable outputs can be obtained if the output mirror is partially transparent for the signal and/or

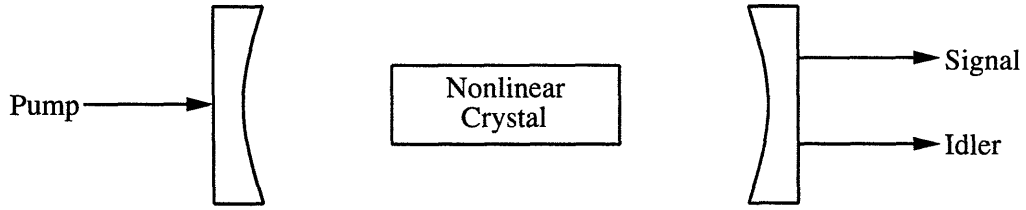

Figure 1-3: Configuration for an optical parametric oscillator.

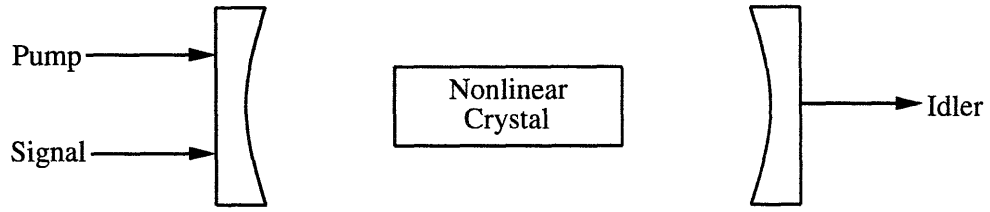

Figure 1-4: Configuration for resonant difference-frequency mixing.

idler.

For a very lossy cavity, a high power pump laser is required to achieve optical parametric oscillation. If such a laser is unavailable, oscillation will not be possible. In this case, a resonant difference-frequency mixing (RDFM) process as shown in Figure 1-4 can be constructed. The configuration for RDFM is similar to that of the OPO except that the RDFM process requires two inputs (the pump and the signal) for tunable operation. For a given crystal and phase-matching configuration, the important parameters for RDFM, as well as DFM, are crystal length, walk-off angle, absorption of the crystal at the interacting wavelengths, nonlinear coefficients of the crystal, and focusing of the pump and the signal.

While an optical parametric oscillator is the more useful application, resonant difference-frequency mixing can provide valuable information on the small signal performance of an OPO. Since optical parametric oscillators are threshold devices, knowledge of the gain in RDFM can improve the design and optimization of an OPO. In addition, RDFM is an attractive tunable source because it can increase the gain of the DFM process by as much as a factor of 1000.

1.3 Thesis Organization

This thesis describes a technique to generate tunable output light at 1.6 μm by difference-frequency mixing in CTA. To increase the generated idler power, the CTA crystal is placed inside a cavity for resonant difference-frequency mixing. Chapter 2 reviews the basic theories of nonlinear optics needed to provide the theoretical background for DFM and RDFM. Chapter 3 presents the theoretical framework for the generation of tunable light by DFM and RDFM in CTA. Chapter 4 outlines the procedures and results of the experiments performed on the proposed DFM and RDFM schemes. Finally, Chapter 5 summarizes the contents of the thesis and suggests further potential research ideas.

Chapter 2

Review

This chapter reviews the relevant topics in electromagnetic wave theory and nonlinear optics for establishing the theoretical foundation of difference-frequency mixing. The main emphasis of this chapter is to derive the system of equations describing the three-wave coupling process in a nonlinear medium which form the basis for the theory of difference-frequency mixing and resonant difference-frequency mixing. First in Section 2.1, we explain the nonlinear interaction between an electromagnetic wave and a medium using a simple classical model. The electric polarization which describes the nonlinear response of the medium to the electromagnetic wave is then introduced in Section 2.2. Next, we present Maxwell's equations in Section 2.3. Maxwell's equations are then used to obtain the wave equation in Section 2.4. The coupled wave equations for the three waves interacting in a nonlinear medium with a second-order nonlinear polarization are derived in Section 2.5. Finally, conservation of energy among the three interacting waves is demonstrated from the coupled wave equations in Section 2.6.

2.1 Theory of Nonlinear Interactions

The nonlinear optical effects for optical parametric generation can be explained by considering the propagation of an electromagnetic wave through a medium. We will use the electron oscillator model to describe the response of the atoms of the medium

when they interact with the electromagnetic wave. Initially, each electron in an atom is in a certain equilibrium state. The incident wave then displaces the electrons from their equilibrium state, inducing oscillating dipole moments. These electric dipoles then immediately serve as secondary sources for new electromagnetic fields. If the energy provided by the incident light is small compared to the binding energy of the electrons, then the dipoles will oscillate and emit radiation at the same frequency as the incident field. As the intensity of the input wave increases to the corresponding energy levels greater than or comparable to the binding energy, the relationship between the intensity of the input field and the amplitude of the dipole oscillations becomes nonlinear. Therefore, the oscillating dipoles will emit radiation at frequencies different from that of the input beam.

2.2 The Nonlinear Polarization

The nonlinear effect due to a sufficiently high intensity field incident upon a medium is characterized by the relationship between the induced electric dipole moment per unit volume $\mathbf{P}$ and the input electric field strength $\mathbf{E}$. If we treat the nonlinear contribution to the interaction as a small perturbation on the linear effects, the polarization of the medium can be expressed as a Taylor series in terms of the electric field within the medium:

$$\mathbf{P} = \hat{\mathbf{p}}_1 \epsilon_0 \chi^{(1)} E + \mathbf{P_{NL}}. \tag{2.1}$$

where the first-order term represents the linear polarization of the medium that is responsible for ordinary optical phenomenon, $\mathbf{P_{NL}} = \epsilon_0[\hat{\mathbf{p}}_2 \chi^{(2)} E^2 + \hat{\mathbf{p}}_3 \chi^{(3)} E^3 + \cdots]$ is the nonlinear polarization induced by the input electric fields in the medium, ϵ_0 is the permittivity of free space, and $\chi^{(m)}$ is the mth-order susceptibility.

For difference-frequency mixing, the nonlinear interactions are second-order. In this case, the nonlinear contribution to the induced polarization is quadratic in the electric field,

$$\mathbf{P_{NL}} = \hat{\mathbf{p}}_2 \epsilon_0 \chi^{(2)} E_1 E_2,$$

where $\chi^{(2)}$ is the second-order optical susceptibility. Since $\chi^{(2)}$ is a three-dimensional tensor, the second-order nonlinear polarization can be expressed as

$$\mathbf{P}_i = \hat{\mathbf{p}}_i \epsilon_0 \sum_{jk} \chi^{(2)}_{ijk} E_j E_k,$$

where i, j, and k each take the coordinate components x, y and z. Conventionally, in experimental optics the nonlinear coefficient tensor d_{ijk} is used instead of $\chi^{(2)}_{ijk}$, which are related by[12]

$$\chi^{(2)}_{ijk} = 2d_{ijk}.$$

In addition, we can further simplify the second-order nonlinear polarization by using a scalar parameter called the effective nonlinear coefficient (d_{eff}). In this case, the second-order nonlinear polarization is[3]

$$\mathbf{P_{NL}} = \hat{\mathbf{p}} 2\epsilon_0 d_{\text{eff}} E_1 E_2, \tag{2.2}$$

where $\hat{\mathbf{p}}$ is the unit vector for the second-order nonlinear polarization. The value of d_{eff} depends on the phase-matching condition (Type I or Type II), the crystal class, and the orientation of the polarization and propagation direction with respect to the optical axis.

2.3 Maxwell's Equations

The basis of electromagnetic wave theory is Maxwell's equations which describe the propagation of electromagnetic waves in any given medium. In mks units, Maxwell's equations in differential form are[21]

Faraday's Law: $$\nabla \times \mathbf{E} = -\frac{\partial \mathbf{B}}{\partial t}$$

Ampere's Law: $$\nabla \times \mathbf{H} = \frac{\partial \mathbf{D}}{\partial t} + \mathbf{J}$$

Gauss's Law for Electric Fields: $$\nabla \cdot \mathbf{D} = \rho$$

Gauss's Law for Magnetic Fields: $$\nabla \cdot \mathbf{B} = 0$$

where $\nabla = \hat{\mathbf{x}}\frac{\partial}{\partial x} + \hat{\mathbf{y}}\frac{\partial}{\partial y} + \hat{\mathbf{z}}\frac{\partial}{\partial z}$ is the del operator, $\mathbf{E}$ is the electric field strength [V/m], $\mathbf{H}$ is the magnetic field strength [A/m], $\mathbf{D}$ is the electric displacement field [C/m^2], $\mathbf{B}$ is the magnetic flux density [W/m^2], $\mathbf{J}$ is the electric current density [A/m^2], and ρ is the electric charge density [C/m^3]. The characteristics of the nonlinear medium is described by the constitutive relations:

$$\mathbf{D} = \epsilon\mathbf{E} \tag{2.3}$$

$$\mathbf{B} = \mu\mathbf{H} \tag{2.4}$$

$$\mathbf{J} = \sigma\mathbf{E} \tag{2.5}$$

where the permittivity ϵ, permeability μ, and conductivity σ are the parameters that characterize the medium. Note that Equation 2.5 is known as Ohm's Law.

For this analysis, we will assume the nonlinear medium is nonconducting and lossless ($\sigma = 0$), free from charge ($\rho = 0$), and nonmagnetic ($\mu = \mu_0$). In this case, Maxwell's equations and the constitutive relations reduce to

$$\nabla \times \mathbf{E} = -\frac{\partial \mathbf{B}}{\partial t} \tag{2.6}$$

$$\nabla \times \mathbf{H} = \frac{\partial \mathbf{D}}{\partial t} \tag{2.7}$$

$$\nabla \cdot \mathbf{D} = 0 \tag{2.8}$$

$$\nabla \cdot \mathbf{B} = 0 \tag{2.9}$$

$$\mathbf{D} = \epsilon_0\mathbf{E} + \mathbf{P} \tag{2.10}$$

$$\mathbf{B} = \mu_0\mathbf{H} \tag{2.11}$$

$$\mathbf{J} = 0 \tag{2.12}$$

where $\epsilon_0 = 8.85 \times 10^{-12}$ F/m and $\mu_0 = 4\pi \times 10^{-7}$ H/m are the permittivity and permeability of free space, respectively. Note that in Equation 2.10 we have expressed $\mathbf{D}$ as a function of the electric polarization $\mathbf{P}$ described in the previous section.

2.4 The Wave Equation

In nonlinear interactions, the propagation of the electric field in a nonlinear medium is described by the wave equation. This equation can be derived from Maxwell's equations. If we take the curl of Equation 2.6 and substitute Equation 2.11 for $\mathbf{B}$, then

$$\nabla \times (\nabla \times \mathbf{E}) = -\mu_0 \frac{\partial}{\partial t}(\nabla \times \mathbf{H}).$$

Using the identity $\nabla \times (\nabla \times \mathbf{E}) = \nabla(\nabla \cdot \mathbf{E}) - \nabla^2 \mathbf{E}$ and Equation 2.7, we obtain

$$\nabla(\nabla \cdot \mathbf{E}) - \nabla^2 \mathbf{E} = -\mu_0 \frac{\partial^2 \mathbf{D}}{\partial t^2}. \tag{2.13}$$

From Equations 2.8 and 2.10, we see that in general $\nabla \cdot \mathbf{E} \neq 0$ when $\mathbf{P}$ exists. However, if we consider only transverse waves where the electric field and polarization are orthogonal to the propagation direction, then $\nabla \cdot \mathbf{E} = 0$. In this case, Equation 2.13 reduces to

$$\nabla^2 \mathbf{E} = \mu_0 \frac{\partial^2 \mathbf{D}}{\partial t^2}.$$

Substituting Equation 2.10 into this equation for $\mathbf{D}$, we get

$$\nabla^2 \mathbf{E} = \mu_0 \epsilon_0 \frac{\partial^2 \mathbf{E}}{\partial t^2} + \mu_0 \frac{\partial^2 \mathbf{P}}{\partial t^2}.$$

Assuming $\mathbf{E}$ and $\mathbf{P}$ are parallel and substituting Equation 2.1 for $\mathbf{P}$, we obtain the wave equation for a nonlinear medium with a driving term due to the nonlinear polarization,

$$\nabla^2 \mathbf{E} - \mu_0 \epsilon_0 \left[1 + \chi^{(1)}\right] \frac{\partial^2 \mathbf{E}}{\partial t^2} = \mu_0 \frac{\partial^2 \mathbf{P_{NL}}}{\partial t^2}. \tag{2.14}$$

This wave equation is the fundamental equation describing the propagation of an electromagnetic wave in any nonlinear medium.

2.5 The Coupled Wave Equations

The three-wave interaction in a nonlinear medium can be described by a set of coupled wave equations which are obtained by solving the wave equation. We will assume the solution to the wave equation is a general quasi-monochromatic wave which can be written as the product of a plane, monochromatic wave and a slowly varying amplitude. For simplicity, we will assume that the three interacting waves are co-propagating along the z direction. (Note that this direction is arbitrary with respect to the crystallographic axes of the nonlinear medium.)

Within the medium, the total electric field can be expressed as a superposition of the electric fields of the three interacting waves,

$$\mathbf{E} = \mathbf{E}_p + \mathbf{E}_s + \mathbf{E}_i, \tag{2.15}$$

where $\mathbf{E}_m$ is the electric field of each interacting wave given by

$$\begin{aligned} \mathbf{E}_m &= \hat{\mathbf{e}}_m E_m(z,t) \\ &= \hat{\mathbf{e}}_m E_m(z) e^{-j(k_m z - \omega_m t)}. \end{aligned} \tag{2.16}$$

Here $E_m(z,t)$ is a slowly varying function of space and time, $E_m(z)$ is the complex field amplitude, $k_m = \sqrt{\omega_m^2 \mu_0 \epsilon}$ is the wave vector, and $\epsilon = \epsilon_0 \left[1 + \chi^{(1)}\right]$ is the effective permittivity of the nonlinear medium. Note that the subscript $m = p, s, i$ denotes the pump, signal and idler, respectively. This notation will be used for the remainder of this thesis.

Similarly, the total nonlinear polarization in the medium for second-order nonlinear interaction is the sum of the individual polarizations of each interacting field,

$$\mathbf{P_{NL}} = \mathbf{P}_p + \mathbf{P}_s + \mathbf{P}_i, \tag{2.17}$$

where $\mathbf{P}_m = \hat{\mathbf{p}}_m P_m(z,t)$ is the second-order nonlinear polarization produced for each

interacting wave and $P_m(z,t)$ are determined using Equations 2.2 and 2.16,

$$P_p(z,t) = 2\epsilon_0 d_{\text{eff}} E_s(z) E_i(z) e^{-j[(k_s+k_i)z-(\omega_s+\omega_i)t]}, \quad (2.18)$$

$$P_s(z,t) = 2\epsilon_0 d_{\text{eff}} E_p(z) E_i^*(z) e^{-j[(k_p-k_i)z-(\omega_p-\omega_i)t]}, \quad (2.19)$$

$$P_i(z,t) = 2\epsilon_0 d_{\text{eff}} E_p(z) E_s^*(z) e^{-j[(k_p-k_s)z-(\omega_p-\omega_s)t]}. \quad (2.20)$$

Substituting Equations 2.15 and 2.17 into the wave equation (Equation 2.14), we obtain three separate expressions for each of the interacting waves given by

$$\hat{\mathbf{e}}_m \left(\frac{\partial^2 E_m(z,t)}{\partial z^2} - 2jk_m \frac{\partial E_m(z,t)}{\partial z} - \mu_0 \epsilon \frac{\partial^2 E_m(z,t)}{\partial t^2} - 2j\mu_0 \epsilon \omega_m \frac{\partial E_m(z,t)}{\partial t} \right) = \hat{\mathbf{p}}_m \mu_0 \left[\frac{\partial^2 P_m(z,t)}{\partial t^2} + 2j\omega_m \frac{\partial P_m(z,t)}{\partial t} - \omega_m^2 P_m(z,t) \right]. \quad (2.21)$$

To simplify this equation, we use the slowly varying amplitude assumptions that

$$k_m \frac{\partial E_m(z,t)}{\partial z} \gg \frac{\partial^2 E_m(z,t)}{\partial z^2},$$

$$\omega_m \frac{\partial E_m(z,t)}{\partial t} \gg \frac{\partial^2 E_m(z,t)}{\partial t^2},$$

and

$$\omega_m^2 \mu_0 P_m(z,t) \gg \omega_m \frac{\partial P_m(z,t)}{\partial t} \gg \frac{\partial^2 P_m(z,t)}{\partial t^2}.$$

Therefore, the slowly varying envelope approximation reduces Equation 2.21 to

$$\hat{\mathbf{e}}_m \left[2jk_m \frac{\partial E_m(z,t)}{\partial z} + 2j\omega_m \mu_0 \epsilon \frac{\partial E_m(z,t)}{\partial t} \right] = \hat{\mathbf{p}}_m \, \omega_m^2 \mu_0 P_m(z,t).$$

For this analysis, we have assumed that $\hat{\mathbf{e}}_m$ and $\hat{\mathbf{p}}_m$ are parallel. As a result, the previous expression simplifies to

$$\frac{\partial E_m(z,t)}{\partial z} + \frac{n_m}{c} \frac{\partial E_m(z,t)}{\partial t} = -\frac{j\omega_m \mu_0 c}{2n_m} P_m(z,t), \quad (2.22)$$

where $n_m = \sqrt{\frac{\epsilon}{\epsilon_0}}$ is the refractive index and $c = \frac{1}{\sqrt{\mu_0 \epsilon_0}} = 3 \times 10^8$ m/s is the speed of

light. In steady-state, $\frac{\partial}{\partial t} \rightarrow 0$ and Equation 2.22 reduces to

$$\frac{\partial E_m(z,t)}{\partial z} = -\frac{j\omega_m \mu_0 c}{2n_m} P_m(z,t). \tag{2.23}$$

Substituting Equations 2.18 to 2.20 into this equation for $P_m(z,t)$, we obtain a set of coupled wave equations:

$$\frac{\partial E_p(z)}{\partial z} = -\frac{j\omega_p}{n_p c} d_{\text{eff}} E_s(z) E_i(z) e^{j\Delta k z} \tag{2.24}$$

$$\frac{\partial E_s(z)}{\partial z} = -\frac{j\omega_s}{n_s c} d_{\text{eff}} E_p(z) E_i^*(z) e^{-j\Delta k z} \tag{2.25}$$

$$\frac{\partial E_i(z)}{\partial z} = -\frac{j\omega_i}{n_i c} d_{\text{eff}} E_p(z) E_s^*(z) e^{-j\Delta k z} \tag{2.26}$$

where $\Delta k = k_p - k_s - k_i$ is the phase mismatch between the interacting waves.

2.6 Energy Conservation

If we first take the complex conjugate of Equation 2.24 and then multiply the three coupled equations (Equations 2.24 to 2.26) by $\frac{n_p E_p(z)}{\omega_p}$, $\frac{n_s E_s^*(z)}{\omega_s}$, and $\frac{n_i E_i^*(z)}{\omega_i}$, respectively, we get

$$\frac{n_p}{\omega_p}\frac{\partial E_p^2(z)}{\partial z} = +\frac{j d_{\text{eff}}}{c} E_p E_s^* E_i^* e^{j\Delta k z}, \tag{2.27}$$

$$\frac{n_s}{\omega_s}\frac{\partial E_s^2(z)}{\partial z} = -\frac{j d_{\text{eff}}}{c} E_p E_s^* E_i^* e^{j\Delta k z}, \tag{2.28}$$

$$\frac{n_i}{\omega_i}\frac{\partial E_i^2(z)}{\partial z} = -\frac{j d_{\text{eff}}}{c} E_p E_s^* E_i^* e^{j\Delta k z}. \tag{2.29}$$

The intensity of each interacting wave is related to its electric field by

$$I_m = \frac{1}{2} n_m c \epsilon_0 E_m^2(z). \tag{2.30}$$

Using this expression, we see that Equations 2.27 to 2.29 are related by

$$\frac{1}{\omega_p}\frac{\partial I_p}{\partial z} = -\frac{1}{\omega_s}\frac{\partial I_s}{\partial z} = -\frac{1}{\omega_i}\frac{\partial I_i}{\partial z}.$$

This equality, known as the Manley-Rowe relations, represents the conservation of photon energy. Each of the three equal terms describes the rate of change of the number of photons at the corresponding frequency. Therefore, difference-frequency mixing as well as other second-order nonlinear processes can be described in terms of a photon model. The DFM process can be viewed as the decay of a pump photon into a signal photon and an idler photon stimulated by the signal radiation. As a result, for every idler photon generated, a pump photon is destroyed and an additional signal photon is also created. Therefore, the DFM process can also be viewed as optical parametric amplification of the signal wave.

Chapter 3

Theory

In this chapter, we present the theory of difference-frequency mixing and resonant difference-frequency mixing. The aim of this chapter is to formulate the equation for calculating the output idler power for DFM and RDFM. In addition, we extend the plane-wave theory of the previous chapter to include the effects of the Gaussian profiles of the beams and Poynting vector walk-off. First, we derive the equation for the generated output idler power by difference-frequency mixing in Section 3.1. Next, the concept of phase-matching is introduced in Section 3.2 to optimize the DFM process. The angle phase-matching condition for DFM in biaxial crystals is then formulated in Section 3.3. Angle phase-matching is limited by the acceptance angle which is discussed in Section 3.4. The coupled wave equations for resonant difference-frequency mixing is then presented in Section 3.5. Using these equations, we derive the equation to determine the maximum output idler power generated by RDFM in Section 3.6. Finally, the expression for calculating the minimum threshold for optical parametric oscillation is derived in Section 3.7.

3.1 The Generated Output Idler Power by DFM

In this section, we derive the expression to calculate the output idler power generated by difference-frequency mixing using the coupled wave equations in Section 2.5. This derivation follows from the theory of nonlinear interaction among three single-

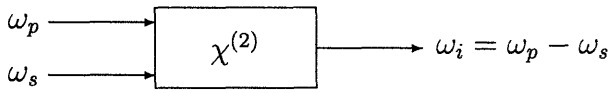

Figure 3-1: Difference-frequency mixing in a second-order nonlinear crystal.

mode electromagnetic fields formulated in a classic paper by Armstrong, et al.[1] The difference-frequency mixing process is schematically shown in Figure 3-1. Assuming negligible pump and signal depletions ($E_p(z) = E_p$ and $E_s(z) = E_s$ are constants along the length of the crystal), we can solve for $E_i(z)$ by simply integrating Equation 2.26 over the entire crystal length:

$$\begin{aligned} E_i(z) &= -\frac{j\omega_i}{n_i c} d_{\text{eff}} E_p E_s^* \int_0^\ell e^{-j\Delta k z} dz \\ &= -\frac{j\omega_i}{n_i c} d_{\text{eff}} E_p E_s^* \ell e^{-j\Delta k \ell/2} \left[\frac{\sin(\Delta k \ell/2)}{(\Delta k \ell/2)}\right]. \end{aligned}$$

Substituting this equation into Equation 2.30, we find that the intensity of the output idler is

$$\begin{aligned} I_i &= \frac{2\omega_i^2 d_{\text{eff}}^2}{c^3 \epsilon_0 n_p n_s n_i} I_p I_s \ell^2 \left[\frac{\sin(\Delta k \ell/2)}{(\Delta k \ell/2)}\right]^2 \\ &= \frac{8\pi^2 d_{\text{eff}}^2}{c \epsilon_0 n_p n_s n_i \lambda_i^2} I_p I_s \ell^2 \left[\frac{\sin(\Delta k \ell/2)}{(\Delta k \ell/2)}\right]^2. \end{aligned}$$

The power of each field can be expressed as $P_m = I_m \mathcal{A}_m$, where $\mathcal{A}_m$ is the transverse beam area. The output idler power is then

$$P_i = \frac{8\pi^2 d_{\text{eff}}^2 \ell^2 P_p P_s \mathcal{A}_i}{c \epsilon_0 n_p n_s n_i \lambda_i^2 \mathcal{A}_p \mathcal{A}_s} \left[\frac{\sin(\Delta k \ell/2)}{(\Delta k \ell/2)}\right]^2. \tag{3.1}$$

The derivation of the coupled wave equations in Section 2.5 was based on the assumption that the electric field for each of the three interacting waves is an infinite uniform plane wave. Therefore, the single-mode beams at the three wavelengths are assumed to be collimated as they propagate through the crystal (i.e., no beam divergence). However, actual laser beams have finite beam divergence. In fact, the

laser outputs for the pump and signal are Gaussian beams. Therefore, the two input beams must be spatially matched and focused at the center of the crystal to optimize the efficiency. The spatial overlap of the two input beams is limited by the requirement that the fields should not be too divergent within the crystal. This condition is satisfied by making the confocal parameter $b = \frac{2\pi n w_0^2}{\lambda}$ equal to or greater than the crystal length.

For confocal parameters greater than the physical crystal length, the electric field in Equation 2.16 can be appropriately modified to take into account the Gaussian beam profile,

$$\begin{aligned} \mathbf{E}_m(r) &= \mathbf{E}_m e^{-r^2/w_m^2} \\ &= \hat{\mathbf{e}} E_m(z,t) e^{-r^2/w_m^2} \end{aligned} \tag{3.2}$$

where w_m is the beam waist that describes the radial dependence of the Gaussian field. Using this equation, we find that the nonlinear polarization $P_m(z,t)$ in Equations 2.18 and 2.20 are given by

$$P_p(z,t) = 2\epsilon_0 d_{\text{eff}} E_s E_i e^{-r^2/\bar{w}_p^2} e^{-j[(k_s+k_i)z-(\omega_s+\omega_i)t]}, \tag{3.3}$$

$$P_s(z,t) = 2\epsilon_0 d_{\text{eff}} E_p E_i^* e^{-r^2/\bar{w}_s^2} e^{-j[(k_p-k_i)z-(\omega_p-\omega_i)t]}, \tag{3.4}$$

$$P_i(z,t) = 2\epsilon_0 d_{\text{eff}} E_p E_s^* e^{-r^2/\bar{w}_i^2} e^{-j[(k_p-k_s)z-(\omega_p-\omega_s)t]}, \tag{3.5}$$

where $\bar{w}_m$ is the beam radius of the driving polarization given by

$$\begin{aligned} \frac{1}{\bar{w}_p^2} &= \frac{1}{w_s^2} + \frac{1}{w_i^2}, \\ \frac{1}{\bar{w}_s^2} &= \frac{1}{w_p^2} + \frac{1}{w_i^2}, \\ \frac{1}{\bar{w}_i^2} &= \frac{1}{w_p^2} + \frac{1}{w_s^2}. \end{aligned}$$

For difference-frequency mixing, the idler wave is free and therefore, assumes the profile of its driving polarization ($w_i = \bar{w}_i$). Therefore, the effect of mixing the two

input Gaussian beams with w_p and w_s produces a polarization with a beam waist given by

$$\frac{1}{w_i^2} = \frac{1}{w_p^2} + \frac{1}{w_s^2}. \tag{3.6}$$

For Gaussian beams in the near-field limit, the effective area is $\mathcal{A}_m = \frac{1}{2}\pi w_m^2$. The derivation of this effective area is found in Appendix A. Substituting this expression of the effective area and Equation 3.6 into Equation 3.1, we can express the output idler power as

$$P_i = \frac{16\pi d_{\text{eff}}^2 \ell^2 P_p P_s}{c\epsilon_0 n_p n_s n_i \lambda_i^2 (w_p^2 + w_s^2)} \left[\frac{\sin(\Delta k\ell/2)}{(\Delta k\ell/2)}\right]^2. \tag{3.7}$$

This undepleted pump and signal approximation represents the maximum idler power that can be generated by difference-frequency mixing.

The analysis so far assumes perfect overlap among the three interacting fields, so that there is no beam walk-off effect caused by the slight refractive-index difference among the three waves. This Poynting vector walk-off or double refraction limits the useful crystal length and thereby reduces the conversion efficiency for difference-frequency mixing. If we now take into account the effects of double refraction for focused Gaussian beams in the theory of Boyd and Kleinman[5], then the generated output idler power by difference-frequency mixing is[8]

$$P_i = \frac{16\pi d_{\text{eff}}^2 P_p P_s \ell \bar{h}_m(B,\xi)}{c\epsilon_0 n_p n_s n_i \lambda_i^2 (\frac{1}{k_p} + \frac{1}{k_s})} \left[\frac{\sin(\Delta k\ell/2)}{(\Delta k\ell/2)}\right]^2, \tag{3.8}$$

where $\bar{h}_m(B,\xi)$ is the reduction factor (to be discussed in the following subsection). In the near-field approximation with negligible walk-off, $\bar{h}_m(B,\xi) \to \xi$, for $\xi < 0.4$ and $\xi < 1/6B^2$. Substituting this limit into Equation 3.8, we obtain the expression without walk-off in Equation 3.7.

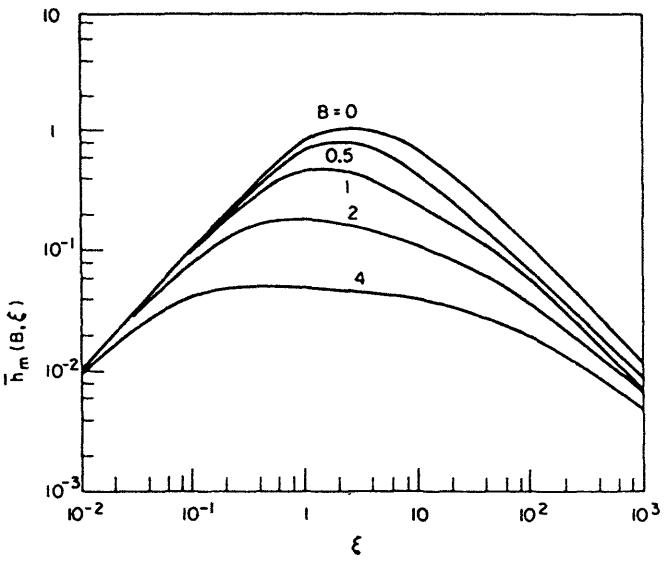

Figure 3-2: The reduction factor $\bar{h}_m(B,\xi)$ as a function of ξ with B as a parameter.

3.1.1 The Reduction Factor

Boyd and Kleinman[5] analyzed the effects of focusing on parametric generation and showed that the Poynting vector walk-off reduces the effective single pass gain by a factor of $\bar{h}_m(B,\xi)$, where $\xi = \ell/b$ is the focusing parameter for the confocal parameter $b = \frac{2\pi n w^2}{\lambda}$ common to all three waves and B is the double refraction parameter defined as

$$B = \frac{\rho}{2}\sqrt{\frac{\ell k_p}{2}}, \tag{3.9}$$

where ρ is the walk-off angle, ℓ is the physical crystal length, and $k_p = \frac{2\pi n_p}{\lambda_p}$ is the pump wave number.

For a given B and ξ, the reduction factor can then be determined from the appropriate graphs plotted by Boyd and Kleinman.[5] The relevant graphs for the DFM parameters in this thesis are shown in Figures 3-2 and 3-3. The optimum reduction factor, shown as the dashed curve in Figure 3-3, can be approximated as[5]

$$\bar{h}_{mm}(B) \approx \frac{\bar{h}_{mm}(0)}{1 + \frac{4B^2}{\pi}\bar{h}_{mm}(0)},$$

where $\bar{h}_{mm}(0) = 1.068$ is the maximum possible value of $\bar{h}_m(B,\xi)$.

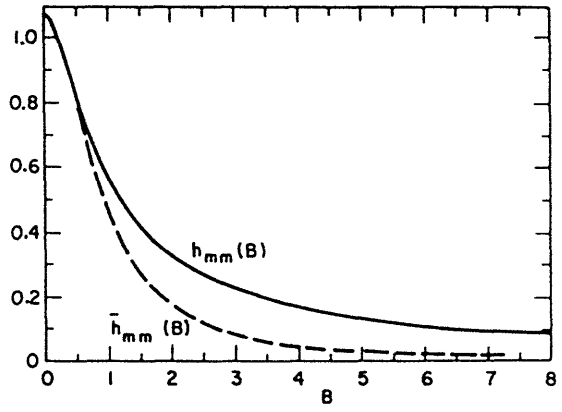

Figure 3-3: The maximum reduction factor for second-harmonic generation $h_{mm}(B)$ and parametric generation $\bar{h}_{mm}(B)$ as a function of B with $\xi = 2.84$.

3.1.2 The Walk-Off Angle

Poynting vector walk-off occurs in nonlinear crystals which exhibit different refractive indices for the three interacting waves. For biaxial crystals, this effect is characterized by a tensorial permittivity ϵ. According to Equation 2.3, if the propagation direction $\mathbf{k}$ is not along one of the optic axes of the biaxial crystal, then $\mathbf{D}$ and $\mathbf{E}$ are at different directions. From Maxwell's equations for a nonmagnetic medium, $\mathbf{D}$, $\mathbf{E}$ and $\mathbf{k}$ lie in the same plane and are orthogonal to $\mathbf{H}$. The Poynting vector $\mathbf{S} = \mathbf{E} \times \mathbf{H}$, which represents the direction of the energy flow, also lies in the same plane as $\mathbf{D}$, $\mathbf{E}$ and $\mathbf{k}$, but is not necessarily parallel to $\mathbf{k}$. Therefore, the energy does not flow in the same direction as the wave propagation. The relative directions of these vectors are shown in Figure 3-4. From geometrical relations of Figure 3-4,

$$\sin\rho = -\hat{\mathbf{e}} \cdot \hat{\mathbf{k}},$$

$$\cos\rho = \hat{\mathbf{e}} \cdot \hat{\mathbf{d}},$$

where ρ is the walk-off angle between $\mathbf{S}$ and $\mathbf{k}$, and $\hat{\mathbf{d}}$, $\hat{\mathbf{e}}$ and $\hat{\mathbf{k}}$ are the unit vectors denoting the directions of $\mathbf{D}$, $\mathbf{E}$ and $\mathbf{k}$, respectively. From these two relations, we see that the walk-off angle is

$$\rho = \tan^{-1}\left(-\frac{\hat{\mathbf{e}} \cdot \hat{\mathbf{k}}}{\hat{\mathbf{e}} \cdot \hat{\mathbf{d}}}\right).$$

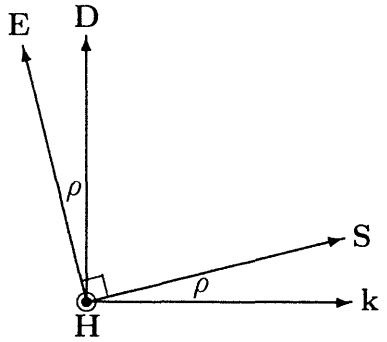

Figure 3-4: The typical directions of the relevant vectors in a biaxial crystal. The walk-off angle is represented by the parameter ρ.

Using the expressions for the cosine vectors of **D** and **E**, Brehat and Wyncke[6] obtain the equation to calculate the Poynting vector walk-off for each interaction beam:

$$\rho_m = \tan^{-1}\left\{n_m^2\left[\left(\frac{k_x}{n_m^{-2}-n_{m,x}^{-2}}\right)^2+\left(\frac{k_y}{n_m^{-2}-n_{m,y}^{-2}}\right)^2+\left(\frac{k_z}{n_m^{-2}-n_{m,z}^{-2}}\right)^2\right]\right\}, \quad (3.10)$$

where k_x, k_y and k_z are the components of the wave vector, n_m is the refractive index, and $n_{m,x}$, $n_{m,y}$ and $n_{m,z}$ are the principal refractive indices of the crystal. These indices can be calculated from the Sellmeier equations in the form

$$n^2(\lambda) = A + \frac{B}{1-(C/\lambda)^2} - D\lambda^2, \quad (3.11)$$

where λ is the wavelength in μm and the constants A, B, C, and D are the Sellmeier coefficients for the crystal of interest. The largest ρ_m calculated from Equation 3.10 is the walk-off angle used in Equation 3.9.

According to Equation 3.8, we can increase the generated output idler power by using a longer crystal. However, when the crystal length increases, the parametric gain will reach a maximum and then decrease. The reason is due to the Poynting vector walk-off. As ℓ becomes larger than the length of the overlapping area of the pump and signal beams in the crystal, an increase in crystal length no longer contributes to the generation of the idler and absorption by the crystal increases. The crystal length at which the peak gain occurs can be approximated by the aperture length defined

as

$$\ell_a = \frac{2\sqrt{\pi}w_0}{\rho}.$$

For a fixed crystal length, w_0 should be chosen so that ℓ_a is of the order of ℓ.

3.2 Phase-Matching

A perfectly phase-matched difference-frequency mixing process requires that conservation of energy and momentum be satisfied:

Energy:	$\omega_i = \omega_p - \omega_s$
Momentum:	$\mathbf{k}_i = \mathbf{k}_p - \mathbf{k}_s$

Note that the momentum conservation condition can be obtained from the coupled wave equations (Equations 2.24 to 2.26) for $\Delta k = 0$. For an ideal phase-matched process, the phase velocities of the pump and signal waves are equal, the relative phase of the polarizations and the waves is constant, and the intensity of the idler wave increases linearly along the length of the nonlinear crystal. If phase-matching is not achieved, wavelength dispersion within the crystal causes the pump and signal to propagate at different velocities. As the two waves propagate through the crystal, they periodically get out of phase and destructive interference occurs. By phase-matching, the conversion efficiency can be increased because the two waves remain in phase to continuously build up the intensity of the output idler. This phase-matching effect on the gain of the difference-frequency mixing process is represented by the wave vector mismatch Δk in the sinc function of Equation 3.8. When $\Delta k = 0$ we have perfect phase-matching and maximum efficiency. As $|\Delta k|$ increases, the gain decreases. Since perfect phase-matching is nearly impossible to achieve in practice, the phase-matching condition for difference frequency mixing may be satisfied as long as $|\Delta k| \leq \pi/\ell$. In this case, the coherence length, defined as the propagation distance before the interacting waves get out of phase, is $\ell_c = \pi/|\Delta k|$.

There are various techniques for phase-matching the three interacting beams. The

most common method is to use the birefringent characteristics of the nonlinear crystal. In a birefringent crystal, the interacting fields can only propagate as ordinary and extraordinary waves. The ordinary waves correspond to the linearly polarized waves that are perpendicular to the plane formed by the main optic axis and the direction of propagation, and the extraordinary waves are parallel to this plane. The refractive indices of these two types of waves depend on the temperature of the crystal and the angle of propagation with respect to the main optic axis. Therefore, the two general techniques used to achieve phase-matching are temperature tuning and angle tuning.

For temperature phase-matching, the propagation direction of the interacting beams is usually chosen to be along one of the optic axes of the crystal to eliminate Poynting vector walk-off. Since the refractive indices vary with crystal temperature, the phase-matching condition can be satisfied by heating or cooling the crystal. For birefringent crystals that cannot be temperature phase-matched, angle phase-matching is achieved by tuning the angle between the direction of propagation and the main optic axis at a fixed crystal temperature to satisfy the phase-matching condition. The angle tuning is done by rotating the crystal or by changing the direction of the input laser beams with respect to the main optic axis.

3.3 Angle Phase-Matching in Biaxial Crystals

In this section, we formulate the Type II phase-matching condition in positive biaxial crystals to determine the phase-matching angle for difference-frequency mixing. A general approach for calculating the phase-matching conditions has been given by Yao and Fahlen[29] for second-harmonic generation and Kaschke and Koch[18] for sum-frequency mixing. Using the same general approach, we will express the phase-matching conditions for difference-frequency mixing in terms of the principal refractive indices of the crystal and the wave vector.

The phase-matching condition for a difference-frequency mixing process is given by

$$k_p - k_s - k_i = 0. \tag{3.12}$$

Since $k_m = \frac{2\pi f_m}{v_m} = \frac{2\pi n_m}{\lambda_m}$, the phase-matching condition can be expresses as

$$\frac{n_p}{\lambda_p} - \frac{n_s}{\lambda_s} - \frac{n_i}{\lambda_i} = 0. \tag{3.13}$$

For a given propagation direction of an electromagnetic wave with wavelength λ_m in a biaxial crystal, only two linearly orthogonally polarized waves with phase velocities $v_m^{(1)}$ and $v_m^{(2)}$ are allowed. The corresponding refractive indices ($n_m^{(1)}$ and $n_m^{(2)}$) of these two phase velocities must satisfy Fresnel's equation

$$\frac{k_x^2}{n_m^{-2} - n_{m,x}^{-2}} + \frac{k_y^2}{n_m^{-2} - n_{m,y}^{-2}} + \frac{k_z^2}{n_m^{-2} - n_{m,z}^{-2}} = 0, \tag{3.14}$$

where $k_x = \sin\theta\cos\phi$, $k_y = \sin\theta\sin\phi$, and $k_z = \cos\theta$ are the components of the wave vector, and $n_{m,x}$, $n_{m,y}$, and $n_{m,z}$ are the principal refractive indices of the crystal. The relationship of the polar angle θ and ϕ describing the propagation direction $\mathbf{k}$ to the principal axes $\mathbf{x}$, $\mathbf{y}$ and $\mathbf{z}$ is shown in Figure 3-5. The polar angle θ is the angle between the $\mathbf{z}$ axis and $\mathbf{k}$, and ϕ is the angle from the $\mathbf{x}$ axis to the projection of $\mathbf{k}$ in the xy plane. The crystal principal refractive indices can be determined from the Sellmeier equations (Equation 3.11).

To obtain the angle phase-matching condition for DFM in positive biaxial crystals, we need to solve Fresnel's equation (Equation 3.14), which can be rewritten as

$$n_m^4 - b_m n_m^2 + c_m = 0, \tag{3.15}$$

where

$$b_m = k_x^2(n_{m,y}^2 + n_{m,z}^2) + k_y^2(n_{m,x}^2 + n_{m,z}^2) + k_z^2(n_{m,x}^2 + n_{m,y}^2)$$

and

$$c_m = k_x^2 n_{m,y}^2 n_{m,z}^2 + k_y^2 n_{m,x}^2 n_{m,z}^2 + k_z^2 n_{m,x}^2 n_{m,y}^2.$$

Using the binomial formula to solve Equation 3.15, we obtain the following two solu-

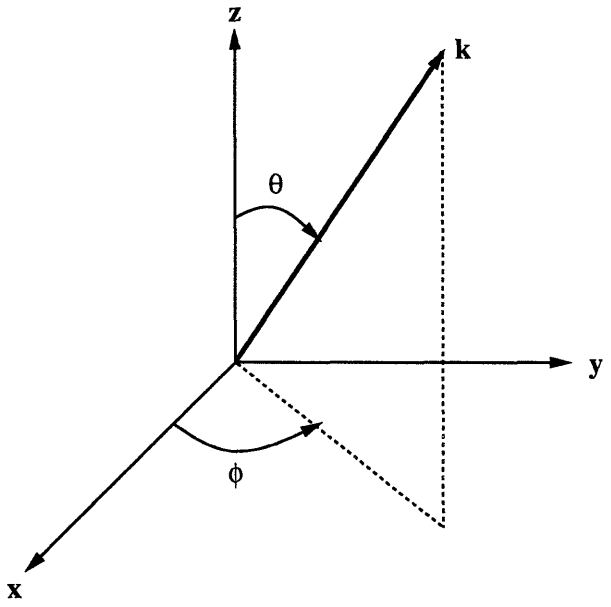

Figure 3-5: The principal axes and polar angles defining the direction of the wave vector **k** in a biaxial crystal.

tions:

$$n_m^{(1)} = \left(\frac{b_m - \sqrt{b_m^2 - 4c_m}}{2} \right)^{\frac{1}{2}}$$

and

$$n_m^{(2)} = \left(\frac{b_m + \sqrt{b_m^2 - 4c_m}}{2} \right)^{\frac{1}{2}}.$$

For Type II phase-matching, the signal and idler waves are orthogonally polarized. From Equation 3.13, the two possible Type II phase-matching conditions for positive biaxial crystals are

$$\frac{n_p^{(2)}}{\lambda_p} - \frac{n_s^{(2)}}{\lambda_s} - \frac{n_i^{(1)}}{\lambda_i} = 0 \tag{3.16}$$

and

$$\frac{n_p^{(2)}}{\lambda_p} - \frac{n_s^{(1)}}{\lambda_s} - \frac{n_i^{(2)}}{\lambda_i} = 0. \tag{3.17}$$

The first condition represents the case where the polarizations of the pump and signal are parallel. Equation 3.17, in which the pump and signal polarizations are perpendicular, is the relevant phase-matching condition for the difference-frequency mixing and resonant difference-frequency mixing experiments in this thesis. For a given com-

bination of λ_p and λ_s, angle phase-matching is achieved by choosing ϕ and θ such that the phase-matching condition is satisfied.

3.4 The Acceptance Angle

An important consideration in angle phase-matching is that the dependence of refractive index on propagation direction used to tune the phase-matching also limits the angular acceptance of the process. The acceptance angle is defined as the angle at which the output idler power decreases to one-half of its peak power.[32] To calculate the angular acceptance, we expand the phase mismatch Δk in a Taylor series about $\phi = \phi_0$, where ϕ_0 is the exact phase-matching angle. For small mismatches,

$$\Delta k(\phi) = \Delta k_0|_{\phi=\phi_0} + \left.\frac{\partial \Delta k}{\partial \phi}\right|_{\phi=\phi_0} \Delta\phi + \frac{1}{2}\left(\frac{\partial^2 \Delta k}{\partial \phi^2}\right)\Bigg|_{\phi=\phi_0} (\Delta\phi)^2 + \cdots$$

For angle phase-matching, the calculation of the acceptance angle depends on the linear term $\partial\Delta k/\partial\phi$. The angular acceptance can then be formulated from the condition that

$$\left[\frac{\sin(\Delta k \ell/2)}{(\Delta k \ell/2)}\right]^2 = 0.5.$$

The solution to this equation, $|\Delta k| = 0.886\pi/\ell$, is at half-width at half-maximum (HWHM). Therefore, the angular acceptance at full-width at half-maximum (FWHM) is

$$\ell\Delta\phi = \frac{1.772\pi}{(\partial\Delta k/\partial\phi)}. \tag{3.18}$$

For a 1 cm long crystal, the acceptance angle is typically several milliradians. Therefore, the angular divergence of the input laser sources for difference-frequency mixing must be minimized and similarly lasers must have narrow linewidths and high spatial coherence.

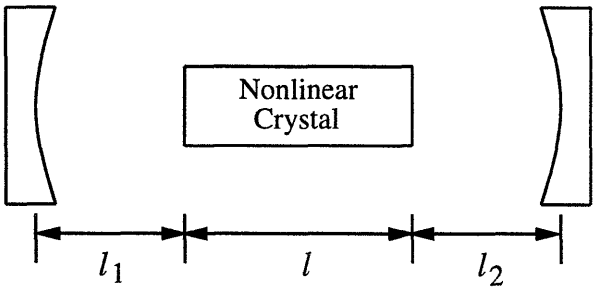

Figure 3-6: Cavity configuration for resonant difference-frequency mixing.

3.5 The Coupled Wave Equations for RDFM

This section derives the coupled wave equations for resonant difference-frequency mixing (RDFM). Consider a doubly-resonant DFM process consisting of a nonlinear crystal inside a linear cavity having a large finesse for the signal and idler fields, but not for the pump field. The configuration of this RDFM process is shown in Figure 3-6. The physical cavity length can be expressed as

$$\ell_{cav} = \ell + \ell_{air},$$

where ℓ is the physical crystal length and $\ell_{air} = l_1 + l_2$ is the free space length of the cavity.

For RDFM, the three interacting waves are linearly polarized fields with Gaussian profiles. To include the effects of the Gaussian beams into the coupled wave equations, we simply substitute Equations 3.3 to 3.5 into Equation 2.23. The coupled wave equations with Gaussian beams are then

$$\frac{\partial E_p(z)}{\partial z} = -\frac{j\omega_p}{n_p c}\frac{2w_s^2 w_i^2 d_{\text{eff}}}{w_p^2 w_s^2 + w_p^2 w_i^2 + w_s^2 w_i^2} E_i(z) E_s(z) e^{j\Delta kz}, \tag{3.19}$$

$$\frac{\partial E_s(z)}{\partial z} = -\frac{j\omega_s}{n_s c}\frac{2w_p^2 w_i^2 d_{\text{eff}}}{w_p^2 w_s^2 + w_p^2 w_i^2 + w_s^2 w_i^2} E_p(z) E_i^*(z) e^{-j\Delta kz}, \tag{3.20}$$

$$\frac{\partial E_i(z)}{\partial z} = -\frac{j\omega_i}{n_i c}\frac{2w_p^2 w_s^2 d_{\text{eff}}}{w_p^2 w_s^2 + w_p^2 w_i^2 + w_s^2 w_i^2} E_p(z) E_s^*(z) e^{-j\Delta kz}. \tag{3.21}$$

To simplify the complexity of these expressions, we normalize the three coupled

equations in terms of photon interaction:

$$\frac{\partial A_p(z)}{\partial z} = -\Gamma A_s(z) A_i(z) e^{j\Delta kz}, \tag{3.22}$$

$$\frac{\partial A_s(z)}{\partial z} = \Gamma A_p(z) A_i^*(z) e^{j\Delta kz}, \tag{3.23}$$

$$\frac{\partial A_i(z)}{\partial z} = \Gamma A_p(z) A_s^*(z) e^{j\Delta kz}, \tag{3.24}$$

where

$$A_m(z) = j \left(\frac{\epsilon_0 n_m \lambda_m \pi w_m^2}{4h} \right)^{\frac{1}{2}} E_m(z)$$

is the complex field amplitude normalized such that $|A_m|^2$ are in units of photons per second, $h = 6.63 \times 10^{-34}$ J·s is Planck constant and

$$\Gamma = \left(\frac{16\pi h d_{\text{eff}}^2}{\epsilon_0 n_p n_s n_i \lambda_p \lambda_s \lambda_i} \right)^{\frac{1}{2}} \frac{2 w_p w_s w_i}{w_p^2 w_s^2 + w_p^2 w_i^2 + w_s^2 w_i^2}$$

is the gain coefficient. According to Boyd and Ashkin[4], the maximum parametric conversion is achieved when

$$\frac{1}{w_p^2} = \frac{1}{w_s^2} + \frac{1}{w_i^2}.$$

In that case, the gain coefficient reduces to

$$\Gamma = \left[\frac{16\pi h d_{\text{eff}}^2}{\epsilon_0 n_p n_s n_i \lambda_p \lambda_s \lambda_i (w_s^2 + w_i^2)} \right]^{\frac{1}{2}}.$$

If we integrate Equations 3.22 to 3.24 over the entire crystal length (from $z = 0$ to $z = \ell$) and consider only the lowest order terms of the field amplitudes, then[11]

$$A_p(\ell) - A_p(0) = -\chi^* A_s(0) A_i(0), \tag{3.25}$$

$$A_s(\ell) - A_s(0) = \chi A_p(0) A_i^*(0), \tag{3.26}$$

$$A_i(\ell) - A_i(0) = \chi A_p(0) A_s^*(0), \tag{3.27}$$

where

$$\begin{aligned}\chi^2 &= \Gamma^2 \ell^2 e^{-j\Delta k\ell} \left[\frac{\sin(\Delta k\ell/2)}{(\Delta k\ell/2)}\right]^2 \\ &= \frac{16\pi h d_{\text{eff}}^2 \ell^2 e^{-j\Delta k\ell}}{\epsilon_0 n_p n_s n_i \lambda_p \lambda_s \lambda_i (w_s^2 + w_i^2)} \left[\frac{\sin(\Delta k\ell/2)}{(\Delta k\ell/2)}\right]^2 \end{aligned} \tag{3.28}$$

is in units of seconds and contains the relevant crystal parameters (d_{eff}, ℓ, n). If we now take into account the effects of the Poynting vector walk-off as analyzed by Boyd and Kleinman, then

$$\chi^2 = \frac{16\pi d_{\text{eff}}^2 h \ell \bar{h}_m(B,\xi) e^{-j\Delta k\ell}}{\epsilon_0 n_p n_s n_i \lambda_p \lambda_s \lambda_i (\frac{1}{k_s} + \frac{1}{k_i})} \left[\frac{\sin(\Delta k\ell/2)}{(\Delta k\ell/2)}\right]^2 . \tag{3.29}$$

Note that if the walk-off is negligible, $\bar{h}_m(B,\xi) \rightarrow \xi$ and Equation 3.29 reduces to Equation 3.28.

To determine the field amplitudes inside the cavity, we modify the coupled wave equations to take into account the gain and losses experienced by the various fields when they propagate inside the cavity. For self consistency, the field at each point in the cavity and the field after one round-trip at the same point must be equal. In this case, the set of coupled wave equations is[11]

$$A_p[1 - r_p(1-\alpha_p)e^{-j\phi_p}] = -\chi^* A_s A_i r_p e^{-j\phi_p} + t_p E_p, \tag{3.30}$$

$$A_s[1 - r_s(1-\alpha_s)e^{-j\phi_s}] = \chi A_p A_i^* r_s e^{-j\phi_s} + t_s E_s, \tag{3.31}$$

$$A_i[1 - r_i(1-\alpha_i)e^{-j\phi_i}] = \chi A_p A_s^* r_i e^{-j\phi_i}, \tag{3.32}$$

where α_m is the percentage of the field amplitude loss due to absorption in the crystal, r_m is the effective field reflection coefficient for the cavity mirrors, $\phi_m = 2k_m(n_m\ell + \ell_{air})$ is the round-trip phase shift inside the cavity, and t_p and t_s are the field transmission coefficients for the input fields E_p and E_s normalized such that $|E_p|^2$ and $|E_s|^2$ are in units of photons per second. Note that for this analysis, we are not considering the phase shifts due to the reflection from the cavity mirrors. Note also that the coupled wave equations derived in Chapter 2 assumed that the nonlinear

medium was lossless ($\sigma = 0$). If the analysis in Section 2.5 had included the effects of a lossy medium, the only modification to the coupled wave equations is an extra loss term which shows up in Equations 3.30 to 3.32 as $\alpha_m A_m$, where α_m is a function of σ.

3.6 The Maximum RDFM Output Idler Power

In this section, we derive the equation to calculate the maximum output idler power that can be generated by resonant difference-frequency mixing. The starting point of this derivation is the coupled wave equations (Equations 3.30 to 3.32). Obviously, the maximum output idler power is generated when all three interacting waves are at resonance ($\phi_m = 2p_m\pi$, where p_m is an integer). In this case, the coupled wave equations for RDFM without cavity detunings are

$$\kappa_p A_p = -\chi^* A_s A_i + t_p E_p, \tag{3.33}$$

$$\kappa_s A_s = \chi A_p A_i^* + t_s E_s, \tag{3.34}$$

$$\kappa_i A_i = \chi A_p A_s^*, \tag{3.35}$$

where $\kappa_m = 1 - r_m(1 - \alpha_m)$ is the percentage of the total field amplitude loss in the cavity. Note that α_m, κ_m, r_m, and t_m are dimensionless parameters ranging from 0 to 1. Assuming no pump depletion, we can reduce the coupled wave equations to

$$A_p = \frac{t_p E_p}{\kappa_p}, \tag{3.36}$$

$$A_s = \frac{\chi A_p A_i^* + t_s E_s}{\kappa_s}, \tag{3.37}$$

$$A_i = \frac{\chi A_p A_s^*}{\kappa_i}. \tag{3.38}$$

Substituting Equations 3.36 and 3.37 into Equation 3.38 for A_p and A_s, and solving for A_i, we get

$$A_i = \frac{\chi t_p E_p t_s E_s^*}{\kappa_p \kappa_s \kappa_i \left(1 - \frac{\chi^2 t_p E_p A_p^*}{\kappa_p \kappa_s \kappa_i}\right)}.$$

If we now substitute Equation 3.36 into this equation for A_p, we obtain an expression for the internal idler field amplitude as

$$A_i = \frac{\chi t_p t_s E_p E_s^*}{\kappa_p \kappa_s \kappa_i \left[1 - \frac{t_p^2 \chi^2 |E_p|^2}{\kappa_p^2 \kappa_s \kappa_i}\right]}.$$

The expected output idler power is then

$$\begin{aligned} P_i &= t_i^2 \frac{hc}{\lambda_i} |A_i|^2 \\ &= \frac{hc}{\lambda_i} \frac{t_p^2 t_s^2 t_i^2 \chi^2 |E_p|^2 |E_s|^2}{\kappa_p^2 \kappa_s^2 \kappa_i^2 \left[1 - \frac{t_p^2 \chi^2 |E_p|^2}{\kappa_p^2 \kappa_s \kappa_i}\right]^2}. \end{aligned} \tag{3.39}$$

Suitable focusing parameters for the RDFM cavity and the input beams can be determined by considering the focused beam waists inside the crystal and the angular acceptance of the crystal. According to Boyd and Ashkin[4], the optimum parametric gain is achieved when the confocal parameters of the pump and signal beams at the center of the crystal are the same. From the calculation of the reduction factor in Section 3.1.1, we see that $\bar{h}_m(B, \xi)$, and therefore the output idler power, increases as the beam waist decreases. However, when the focused beam waist decreases, the angular divergence of the laser source becomes larger than the acceptance angle of the crystal, reducing the gain of the RDFM process.

3.7 The Threshold for Parametric Oscillation

Since the RDFM cavity can provide resonances for both the signal and idler waves, at a particular threshold pump power, the parametric gain will cause simultaneous

oscillation at both the signal and idler frequencies. The threshold for this oscillation corresponds to the point at which the parametric gain just balances the losses of the signal and idler waves. We can use the coupled wave equations to determine this oscillation condition for the doubly resonant optical parametric oscillator. Since the minimum threshold occurs for $\delta_m = 0$ (no detunings), the coupled wave equations for an OPO assuming negligible pump depletion are

$$\kappa_p A_p = t_p E_p, \tag{3.40}$$

$$\kappa_s A_s = \chi A_p A_i^*, \tag{3.41}$$

$$\kappa_i A_i = \chi A_p A_s^*. \tag{3.42}$$

If we multiply Equation 3.41 by the conjugate of Equation 3.42, we get

$$A_p^2 = \frac{\kappa_s \kappa_i}{\chi^2}.$$

Substituting this expression into Equation 3.40, we find that the minimum pump threshold is

$$E_p^2 = \frac{\kappa_p^2 \kappa_s \kappa_i}{t_p^2 \chi^2}.$$

Therefore, the minimum pump power threshold for optical parametric oscillation is

$$P_p^{th} = \frac{hc}{\lambda_p} \frac{\kappa_p^2 \kappa_s \kappa_i}{t_p^2 \chi^2}. \tag{3.43}$$

Chapter 4

Experiments

Experiments are performed to generate tunable continuous-wave output at 1.6 μm by difference-frequency mixing in CTA. After the DFM experiment is completed, the CTA is enclosed in a resonator to perform the RDFM experiment. This chapter describes the procedures and presents the results of these two experiments. For both experiments, the krypton-ion laser serves as the pump and the Ti:sapphire ring laser is the source for the input signal. These two laser systems are described in Sections 4.1 and 4.2. Next, we present in Section 4.3 the optical characteristics of the CTA crystal used in the experiments. The procedures and results of the DFM and the RDFM experiments are then presented in Sections 4.4 and 4.5, respectively.

4.1 The Krypton Laser

The pump laser source is provided by the fundamental mode output of a commercial cw krypton-ion laser (Coherent, Innova 200) at $\lambda_p = 530.9$ nm. An alternative to the krypton laser is the frequency-doubled Nd:YAG laser at $\lambda = 532$ nm. The krypton laser consists of a two mirror linear cavity as shown in Figure 4-1. The laser gain medium is contained in a tube filled with ionized krypton gas. The ends of the tube are at Brewster's angle to reduce losses and to obtain linearly polarized output light. The krypton ions are excited by passing an electric current through the gas along the length of the tube.

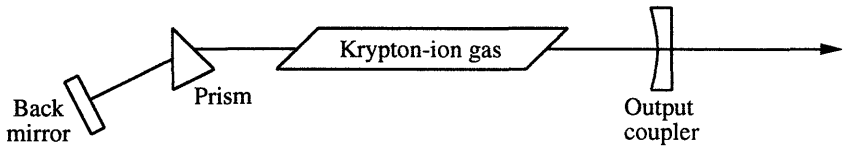

Figure 4-1: The krypton-ion laser.

The krypton laser can operate with one line or multiple lines. For single-frequency operation, the krypton laser cavity contains a prism which bends light of different wavelengths at different angles. At a fixed back mirror position, only one wavelength is bent at the proper angle to oscillate back and forth between the cavity mirrors. All other wavelengths are reflected out of the laser cavity by the back mirror, preventing oscillation at those wavelengths. The prism and the back mirror in combination can then be tuned to select the output wavelength.

The krypton-ion laser system is shown in Figure 4-2. The single-frequency output of the krypton laser passes through a Faraday isolator which is used to block any optical feedback from entering the laser cavity. Such a device is especially necessary for the RDFM experiment since a large percentage of the input light is reflected back from the RDFM cavity. The isolator consists of two polarizers and a Faraday rotator as shown in Figure 4-2. Light in the forward direction is linearly polarized by the input polarizer P1. The plane of polarization is then rotated 45° by the Faraday rotator. Since the output polarizer is oriented at 45° to the input polarizer, the light exits the isolator with very little attenuation, but its linear polarization is at 45° with respect to the input light. In the backward direction, the reflected light will be linearly polarized at an angle of 45° after passing P2. Due to its nonreciprocal property, the Faraday rotator then turns the plane of polarization another 45° so that now the polarization is 90° with respect to P1. As a result, the reflected light is totally rejected by P1. The Faraday isolator used in the experiments provides 40 dB (0.01%) isolation.

The electro-optic modulator (EOM) is used to stabilize the intensity of the krypton laser output. When an electric field is applied across an electro-optic crystal, the refractive index of the crystal changes. A linearly polarized light passing through

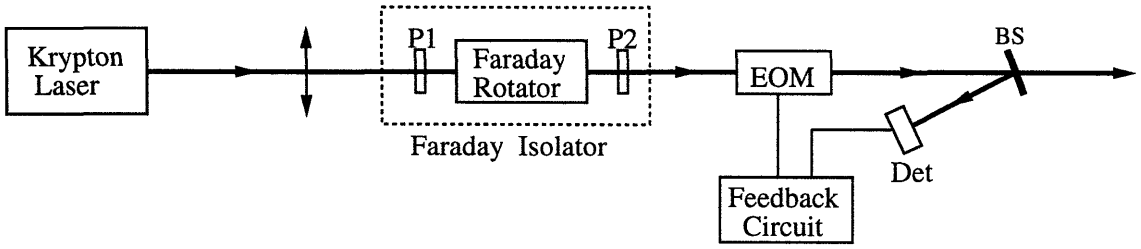

Figure 4-2: The krypton laser system.

the crystal will then be elliptically polarized. If we denote the plane of polarization of the input light as the xy plane and the linear polarization as in the x direction, then the phase shifts for the x and y components depend on the applied voltage. A polarizer oriented at right angles to the polarization of the input beam blocks the x component. The intensity of the transmitted light therefore depends on the ellipticity of the polarization which can be altered by varying the applied field. To stabilize the intensity, a small percentage of the output light is reflected by the beamsplitter (BS) into a photodetector. The DC voltage from this detector is compared to a voltage reference and the feedback circuit provides the appropriate voltage across the electro-optic crystal so that the detected intensity is locked to the reference. We can then obtain intensity-stabilized krypton laser output at various power levels by varying the voltage reference.

4.2 The Ti:Sapphire Laser

The laser source for the input signal is a home-built cw titanium-doped sapphire ring laser whose single-frequency output is tunable from $\lambda_s = 770 - 810$ nm (near infrared region). An alternative source to the Ti:sapphire laser is the dye laser. Since the Ti:sapphire laser is a solid-state laser, it is more convenient to use and intrinsically more stable than dye lasers. Therefore, the Ti:sapphire laser has now replaced the dye laser as the preferred source for the wavelength range from $700 - 1100$ nm.

A ring cavity configuration is chosen for single-frequency operation since spatial hole burning is eliminated for unidirectional operation.[25] Therefore, the Ti:sapphire laser consists of a four mirror astigmatically compensated ring cavity as shown in

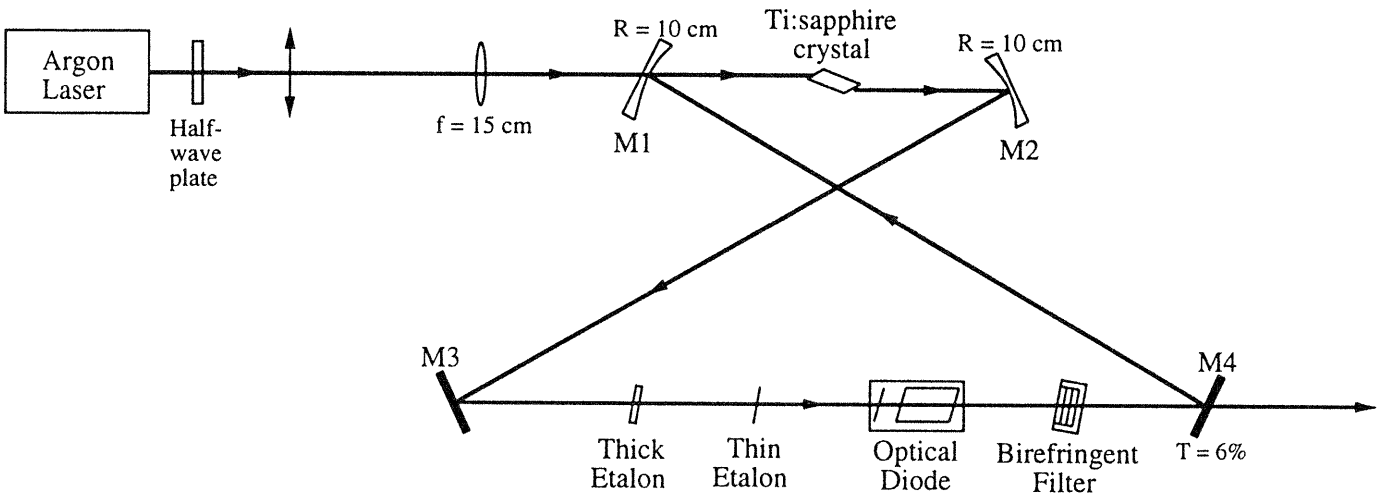

Figure 4-3: The Ti:sapphire ring laser.

Figure 4-3. M1 serves as the input coupler for the argon pump and M2 is a high reflector for the intracavity wavelengths. Since M1 and M2 are both spherical mirrors with 10 cm radius of curvatures, they produce astigmatic Gaussian beams that have different spot sizes, wavefront curvatures, and beam waist positions in the two orthogonal directions. Therefore, the two mirrors are positioned such that the angle of incidence at each mirror is 15° for astigmatism compensation.[19] M3 is a high reflector flat mirror and M4 is a flat mirror that serves as the 6% output coupler for the Ti:sapphire laser output. The total cavity length is 120 cm which corresponds to a free spectral range (FSR) of 250 MHz. Finally, the elements of the cavity are mounted on a small aluminum table (75 cm × 38 cm × 2.5 cm) isolated from the principal optical table with rubber spacers.

The pump source for the Ti:sapphire laser is a commercial cw argon-ion laser (Spectra-Physics, Model 2030-18) operating at all lines from $\lambda = 460 - 514$ nm which covers most of the main absorption bands of Ti:Al_2O_3 between $\lambda = 450 - 550$ nm (blue-green region). The polarization of the argon laser output is made horizontal by passing the beam through a half-wave plate. This horizontally polarized beam is then focused through M1 into the Ti:sapphire crystal using a plano-convex lens with 15 cm focal length to mode match the argon beam to the mode of the Ti:sapphire cavity. To optimize the output power, the Ti:sapphire cavity is configured such that the beam waists are at the center of the Ti:sapphire crystal with $b = 1.7$ cm and at the midpoint between M3 and M4 with $b = 90.3$ cm.

The intracavity elements of the Ti:sapphire ring cavity consists of a Brewster-cut Ti:Al_2O_3 crystal, an optical diode, a three-plate birefringent filter, a thick etalon, and a thin etalon. The Ti:sapphire laser gain medium is a crystal of sapphire (Al_2O_3) doped with titanium (Ti^{3+}) ions.[22] The sapphire host does not participate directly in the lasing action, while the Ti^{3+} ions provide the energy levels for both the pumping and lasing transitions. The Ti:Al_2O_3 crystal was manufactured by Union Carbide for 0.05% Ti^{3+} dopant concentration by atom percent and Brewster-cut at $\theta_B = 60.255°$ to reduce losses for the horizontally polarized waves in the cavity. The dimensions of the crystal are 3 mm in diameter and 2 cm in length.

For a ring laser, intracavity wave propagation can occur in two directions. Due to the homogeneously broadened gain characteristics of Ti:Al_2O_3, the travelling waves in the cavity can couple out at either direction, causing unstable and unreliable output for each direction. To eliminate this problem, an optical diode consisting of a Faraday rotator and an optical rotator is used to ensure unidirectional oscillation.[17] The Faraday rotator is a 12 mm long Brewster-cut piece of Faraday material placed inside a magnetic field to provide nonreciprocal rotation. The optical rotator is a thin, optically active plate used to provide reciprocal rotation. When these two rotators are used in combination, the polarization rotations cancel in the forward propagating direction, while the rotations add for the backward direction. Therefore, the loss for the forward wave is unaffected since its horizontal polarization is unchanged. However, the backward wave is no longer horizontally polarized, and experiences a net loss since its vertical field component is reflected at the many Brewster-angle surfaces in the cavity. A rotation of a few degrees is sufficient to create the small loss difference between the forward and backward waves needed to allow the forward wave to oscillate, and suppress the oscillation of the backward wave.

Since the gain curve of Ti:Al_2O_3 is broad, many oscillation wavelengths can fall under the gain bandwidth. Therefore, selective elements (birefringent filter, thick etalon and thin etalon) are used to obtain single-frequency operation of the Ti:sapphire ring laser. The three-plate birefringent filter is used for broad wavelength tuning.[31] Each plate is made of quartz, with its optic axis in the plane of the plate, and are oriented such that the angle of incidence is at Brewster's angle. When the intracavity beam propagates through a birefringent plate, the incident horizontally polarized light is transformed into elliptically polarized light due to the phase difference between the ordinary and extraordinary waves. The phase difference and therefore the eccentricity of the elliptical polarization depends on the wavelength. After these elliptically polarized waves propagate through the plates and other Brewster surfaces in the cavity, they will experience reflection losses. As a result, those wavelengths whose phase difference is an integral multiple of 2π are not transformed through the birefringent plates, remain horizontally polarized, and encounter minimum loss. One of these

wavelengths will suffer the lowest overall loss and this wavelength is the selected lasing wavelength. A new wavelength can then be selected by rotating the quartz plates about the axis orthogonal to the face of the plates. The birefringent filter used in this Ti:sapphire laser can tune wavelengths every 2.2 nm.

The thick etalon is used to isolate the Ti:sapphire laser output to a single-frequency and for fine wavelength tuning. The etalon is a 5 mm thick piece of glass coated for 20% reflection on both sides with a FSR of 20 GHz. The interference effects of the thick etalon provide discriminating loss to all the possible oscillating wavelengths except one. Therefore, the etalon acts as a bandpass filter, introducing enough loss in all other modes to suppress oscillations at their corresponding wavelengths. By tilting the etalon, we can provide a lower loss to another mode, thereby tuning the oscillating wavelength (about every 0.1 nm).

The main purpose of the thin etalon is to prevent mode-hopping of the laser output from one oscillating mode to another. The etalon is a 0.11 mm thick fused silica plate with a FSR of 900 GHz. Since the two surfaces of the etalon are uncoated, the thin etalon provides a small, but additional loss to all the modes except the oscillating mode. The etalon can also be used in conjunction with the thick etalon for fine wavelength tuning.

The single-frequency cw output of the Ti:sapphire laser is horizontally polarized and broadly tunable from 770−810 nm (near infrared spectral region) with a linewidth of 4 MHz. The Ti:sapphire laser threshold is about 1.5 W of argon laser power and the Ti:sapphire output power versus the pump power is shown in Figure 4-4. The output of the Ti:sapphire laser passes through an optical diode to prevent reflected light from coupling back into the Ti:sapphire cavity and an electro-optic modulator (EOM) which is used for intensity stabilization of the output beam. A small percentage of the output power is then reflected by the beamsplitter (BS) to a wavemeter (Burleigh) and a spectrum analyzer (Newport, Model SR-140-C) to determine the wavelength and frequency stability of the Ti:sapphire laser output. The Ti:sapphire laser system, shown in Figure 4-5, is very similar to the krypton laser system described in the previous section.

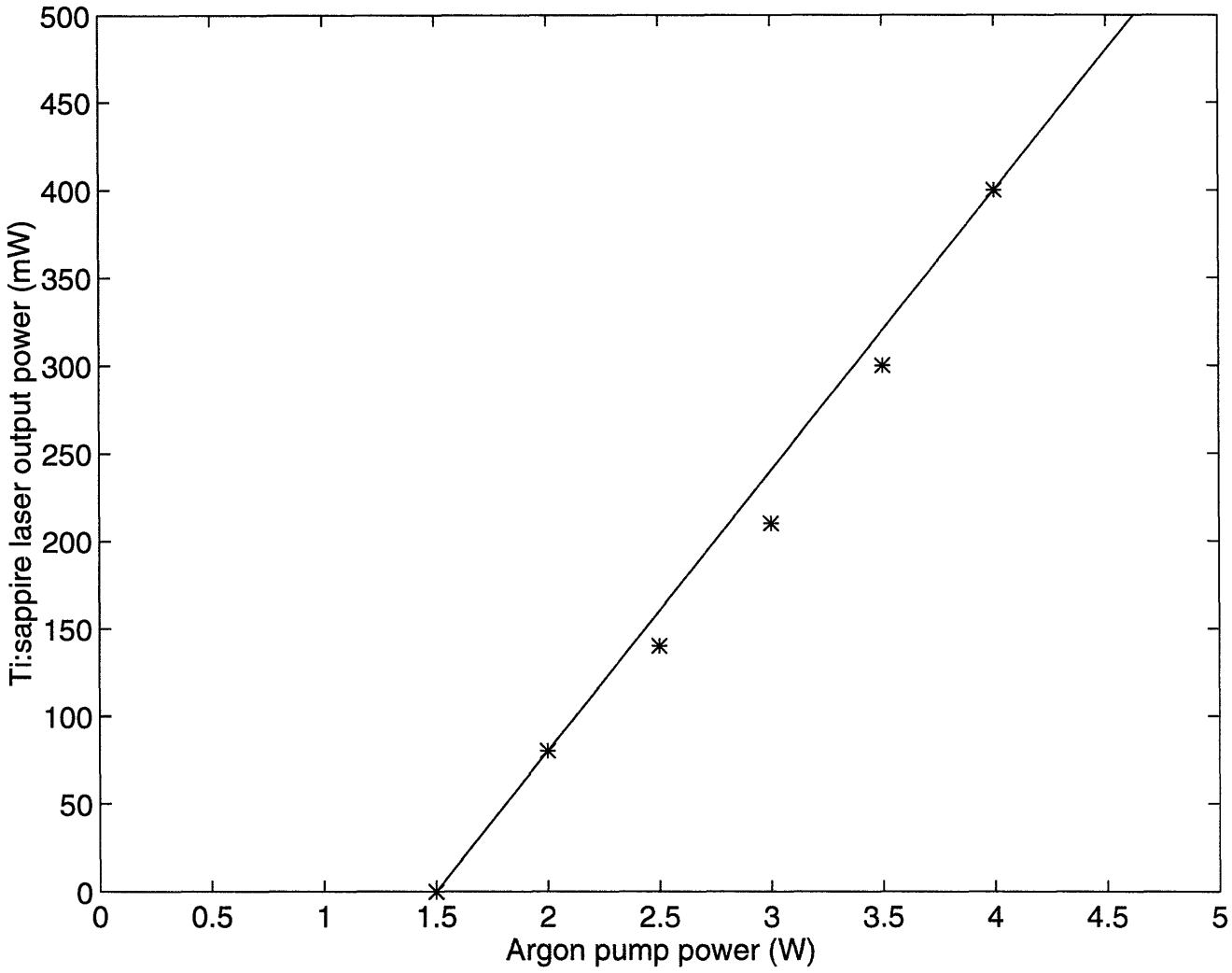

Figure 4-4: The Ti:sapphire ring laser output power as a function of the input pump power from the argon laser. The astericks represent the measured data.

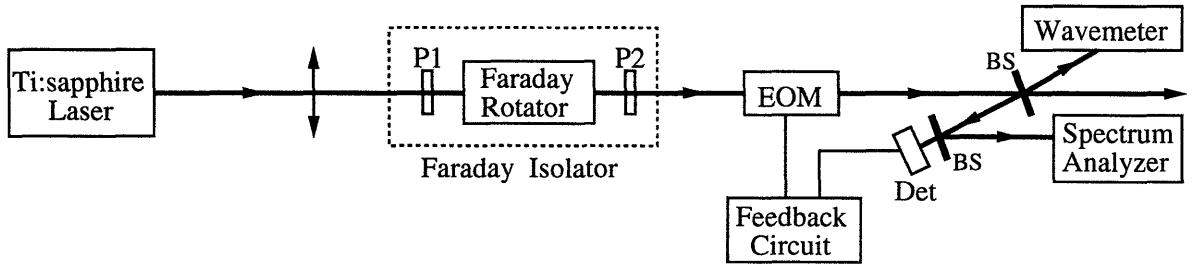

Figure 4-5: The Ti:sapphire laser system.

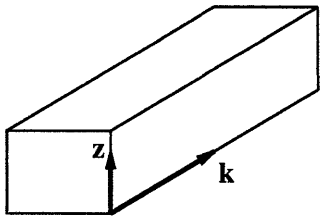

Perspective View

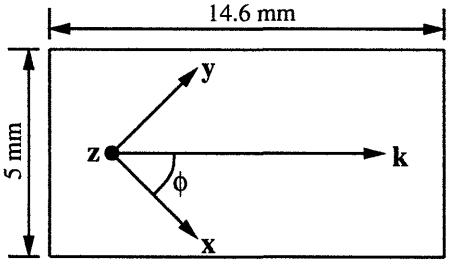

Top View

Figure 4-6: The geometry of the CTA crystal with crystal dimensions and orientation.

4.3 The CTA Crystal

The CTA crystal used in the difference-frequency mixing and the resonant difference-frequency mixing experiments was grown by DuPont.[9] The dimensions of the crystal are 5 mm × 5 mm × 14.6 mm as shown in Figure 4-6. It was cut for Type II phase-matching in the xy plane ($\theta = 90°$) at an internal propagation angle of $\phi = 46.0° \pm 1°$. The two end faces are polished and antireflection coated for the three interacting wavelengths. The measured single-pass transmission through the CTA crystal are 64.3% at $\lambda_p = 530.9$ nm, 99% at $\lambda_s = 790.0$ nm, and 98% at $\lambda_i = 1530.0$ nm. Note that although some of the transmission loss can be attributed to the antireflection coatings at the two end faces, the absorption of the three interacting wavelengths by the CTA crystal is relatively high as compared to that of most nonlinear crystals which exhibit absorptions of only a few tenths of a percent. Since CTA is a new nonlinear crystal, its growth process has not been perfected, resulting in crystal quality that is less than ideal. For the single-pass difference-frequency mixing process, the large absorption does not significantly affect the output idler power. However, for resonant difference-frequency mixing, the absorption can reduce the parametric gain by as

much as a factor of 100.

The three principal refractive indices for CTA are determined from the Sellmeier equations at room temperature given by Cheng, et al.[10]

$$n_x^2(\lambda) = 2.34498 + \frac{1.04863}{1-(0.22044/\lambda)^2} - 0.01483\lambda^2, \tag{4.1}$$

$$n_y^2(\lambda) = 2.74440 + \frac{0.70733}{1-(0.26033/\lambda)^2} - 0.01526\lambda^2, \tag{4.2}$$

$$n_z^2(\lambda) = 2.53666 + \frac{1.10600}{1-(0.24988/\lambda)^2} - 0.01711\lambda^2, \tag{4.3}$$

where λ is expressed in μm. As an example, the principal refractive indices for the three interacting wavelengths of the RDFM experiment are as follows:

λ (nm)	n_x	n_y	n_z
530.9	1.899	1.916	1.988
790.0	1.864	1.878	1.938
1618.7	1.837	1.852	1.904

In the xy plane ($\theta = 90°$), the effective second-order nonlinear coefficient for Type II phase-matching is[28]

$$d_{\text{eff}} = -(d_{15}\sin^2\phi + d_{24}\cos^2\phi).$$

The derivation of this expression is done in Appendix B. The CTA nonlinear coefficients, determined using the Maker fringes technique at 1.064 μm by Cheng, et al., are $d_{15} = d_{31} = 2.1$ pm/V, $d_{24} = d_{32} = 3.4$ pm/V, and $d_{33} = 18.1$ pm/V each with $\pm 20\%$ uncertainty.[10] The d_{eff} plot for Type II phase-matching in the xy plane is shown in Figure 4-7.

The Poynting vector walk-off angles (calculated from Equation 3.10) and the acceptance angles (calculated from Equation 3.18) for Type II phase-matching in the xy plane of the CTA crystal are plotted in Figures 4-8 and 4-9, respectively. For the DFM and RDFM experiments, the calculated walk-off angle is $\rho \approx 0.49°$ (8.55×10^{-3} radians) and the acceptance angle is about 36 milliradians for $\ell = 14.6$ mm.

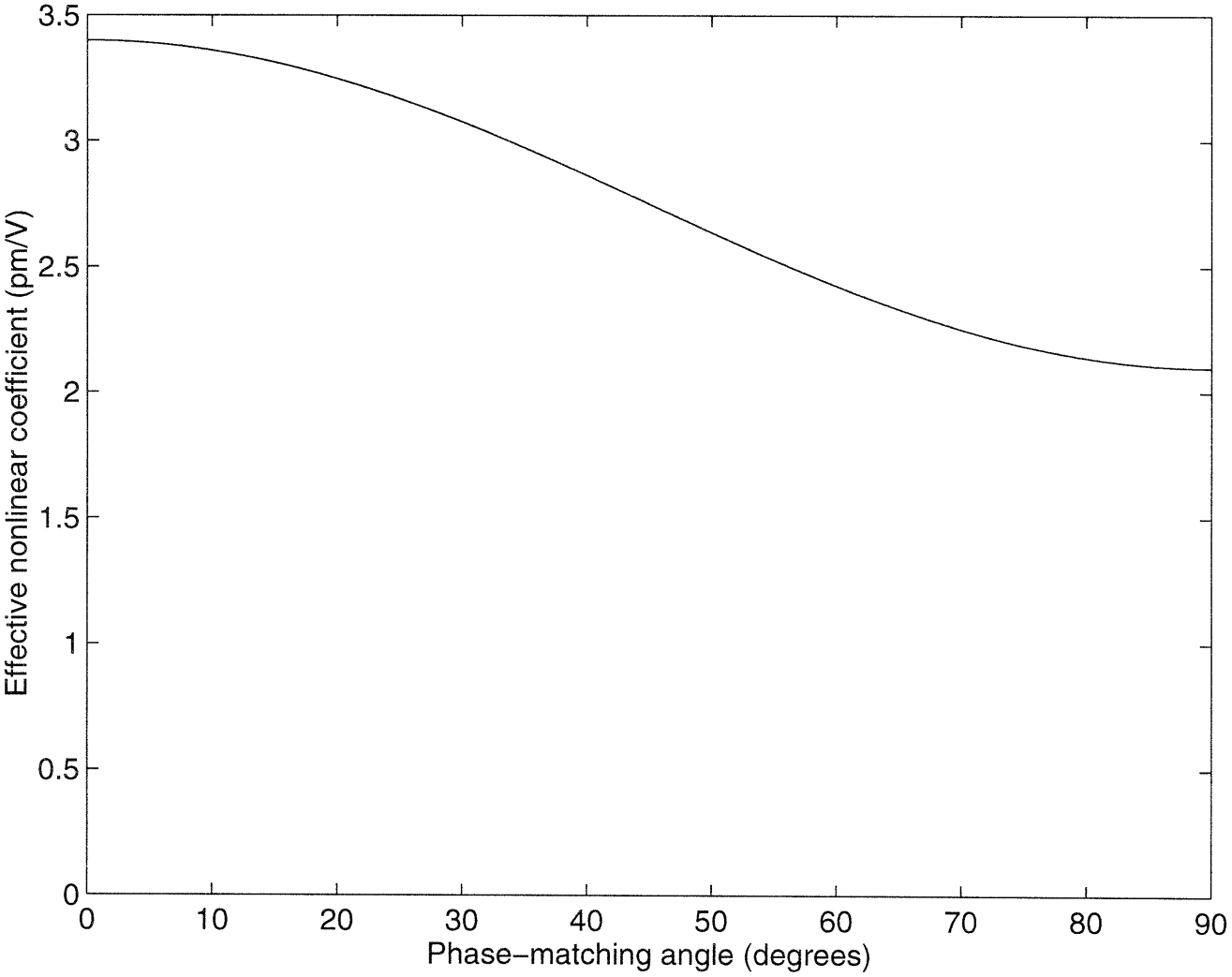

Figure 4-7: The Type II effective nonlinear coefficient (d_{eff}) in the xy plane for CTA as a function of the phase-matching angle ϕ.

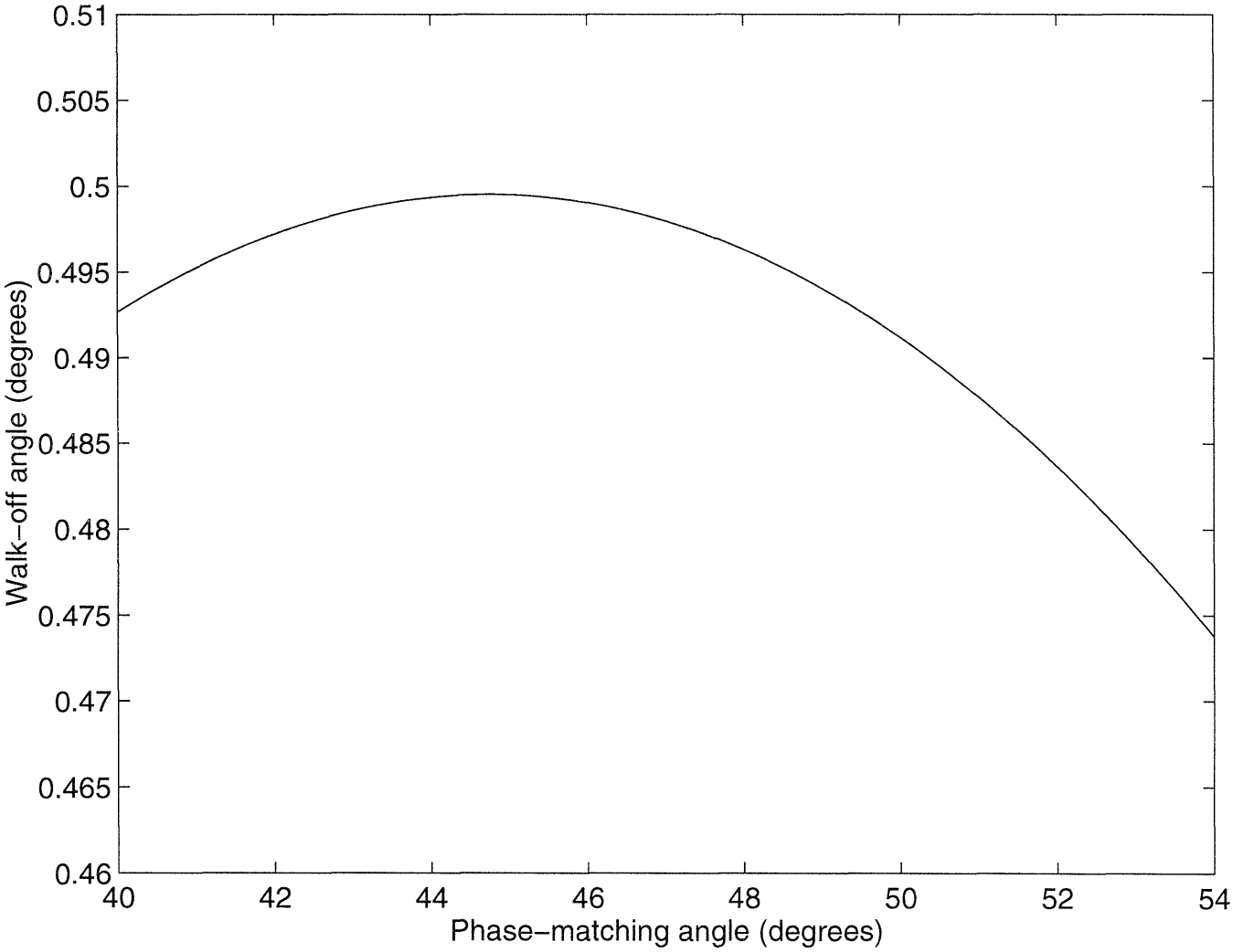

Figure 4-8: The CTA crystal Poynting vector walk-off angle as a function of the phase-matching angle ϕ for $\theta = 90^{\circ}$ and $\lambda_p = 530.9$ nm.

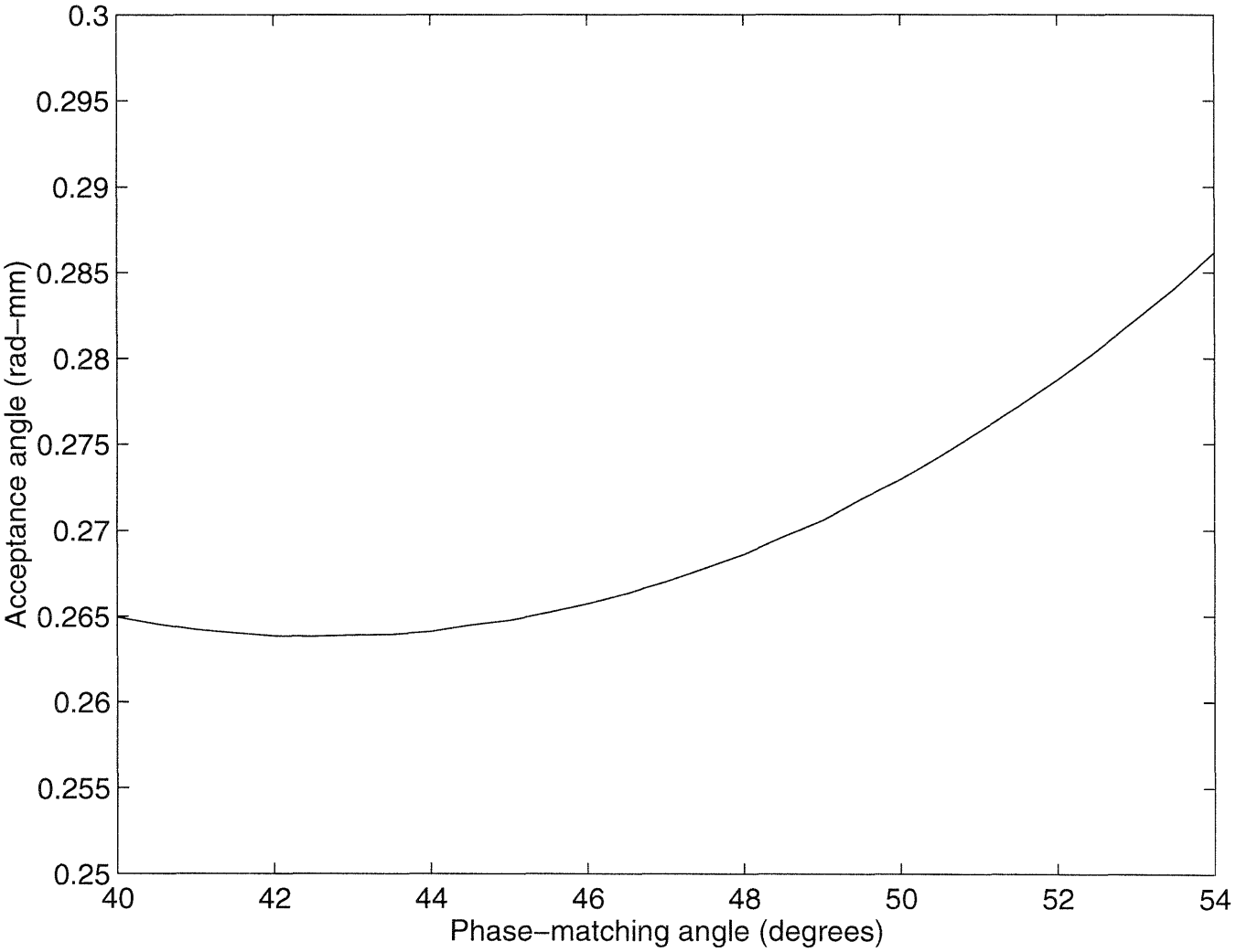

Figure 4-9: The Type II acceptance angle ($\ell\Delta\phi$) in the xy plane for CTA as a function of the exact phase-matching angle ϕ.

4.4 The DFM Experiment

4.4.1 Experimental Setup

This subsection describes the setup to perform the CTA difference-frequency mixing experiment. The experimental setup is schematically shown in Figure 4-10. The crystal was mounted on a small rotation stage (Newport, Model MT-RS) which was on top of a five-axis aligner (New Focus, Model 9081), so that both the angle and position of the crystal could be adjusted. The z-axis of the CTA crystal was in the vertical direction and the incident angle of the input laser beams was changed in the ϕ direction for tuning. The quarter-wave and half-wave plates in combination were used to transform the input beams to the desired polarization. The waveplates were slightly tilted for nonnormal incidence to eliminate the back reflections from the plates into the laser cavity. For the crystal orientation shown in Figure 4-6, the waveplates were adjusted such that the pump was horizontally polarized (perpendicular to the z-axis) and the input signal was vertically polarized (parallel to the z-axis) to satisfy Type II phase-matching. Therefore, the output idler must be horizontally polarized. The pump and signal beams were focused using plano-convex lenses (L1 and L2) with focal lengths of 25 cm and 20 cm, respectively. These lenses, mounted on three-axis translation stages, were positioned such that the focus was at the center of the crystal with a confocal parameter of $b = 1.75$ cm. The corresponding beam waists were then $w_p = 28$ μm, $w_s = 34$ μm, and $w_i = 21$ μm.

The polarizing beamsplitter (PBS) was used to combine the two orthogonally polarized input beams into the CTA crystal. The three beams leaving the crystal then encountered a high-pass filter (made of Schott colored glass) for wavelengths above 830 nm which transmitted the idler beam while blocking the pump and signal beams. Since one filter leaked a bit of the signal beam, two filters were needed to completely block the signal beam. The divergent idler beam was then focused by a bi-convex lens (L3) with 25.4 cm focal length into the InGaAs photodetector coupled to a transimpedance amplifier with 500 kΩ feedback resistance.

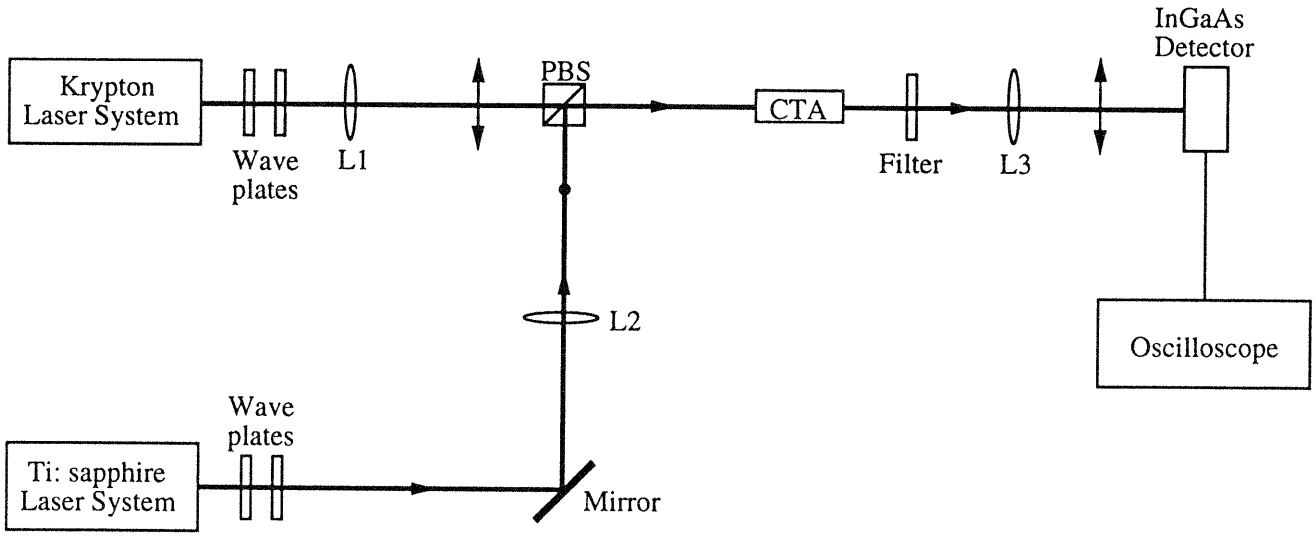

Figure 4-10: Experimental setup for difference-frequency mixing.

4.4.2 Experimental Procedures

This subsection gives a detail account of the alignment and optimization procedures to obtain the maximum output idler power by difference-frequency mixing in CTA. Without the mode-matching lens L1 in place, we adjusted the relevant mirrors so that the pump beam passed straight through the CTA crystal. The same procedure was done for the signal beam with L2 taken out. When L1 and L2 were inserted into the proper positions, the pump and signal beams should propagate through the crystal more or less parallel to each of the four side faces of the crystal. Next, we adjusted the five-axis aligner such that the input beams were reflected directly back from the front end of the crystal.

As an initial check of the mode-matching, we adjusted L1 and L2 such that the input beams propagated through air right above the CTA crystal. The adjustments of the mode-matching lens were along three directions. For the sake of clarity, we will refer to the adjustments from left and right as in the x direction, up and down as in the y direction, and forward and backward as in the z direction. In this case, the previous procedure was accomplished by adjusting L1 and L2 in the y direction. For proper mode-matching, we then adjusted L1 and L2 in the z direction such that the foci of the two beams were located at the same spot about halfway between the front end and the center of the crystal. In addition, the pump and signal beams should have comparable spot sizes at every position after the polarizing beamsplitter.

After the pump and signal beams were suitably mode-matched, we then proceeded to adjust L1 in the x and y directions to find a spot in which the pump beam passed through the crystal without distortions. When this spot was found, L1 was then kept fixed at that position. We next adjusted L2 in the x and y directions so that the signal beam spatially overlapped the pump beam at various points after the polarizing beamsplitter. Without the high-pass filter in place, we now used the signal beam to align L3 to optimally focus light into the InGaAs photodiode.

After this alignment was completed and the filter was back in place, we then tuned the crystal to the calculated ϕ position for the chosen signal wavelength. If the pump

and signal beams were well mode-matched, then output idler power was detected by finely rotating the crystal in the ϕ direction. In this case, we rotated the crystal to the position which generated the most power and then iteratively adjusted L1 and L2 in the x, y and z directions to optimize the generated output idler power.

If the output idler power was not generated by tuning the crystal, then we needed to better mode-match the two input beams. First, we rotated the crystal back to the calculated ϕ position. Without adjusting L1, we iteratively adjusted the x and y positions of L2 to spatially overlap the signal beam to the pump beam. If output idler power was still not generated, the crystal needed to be tuned iteratively with L2 as well. The adjustments of L2 and the crystal positions was sufficient to generate some output idler power. When output idler was detected, small adjustments of L1 and L2 in the x, y and z directions and fine tuning of the crystal in the ϕ direction would optimize the output power.

After the optimization was completed, the angle of incidence of the input beams at the front end of the crystal was noted and the generated output idler powers were recorded for various input pump and signal power levels. The Ti:sapphire laser output was then tuned to a different wavelength by tuning the birefringent filter and thick etalon. Since the pump and signal beams were well mode-matched, rotating the crystal in the ϕ direction was sufficient to generate the output idler for this new signal wavelength. If necessary, the same procedures mentioned earlier was used to optimize the output idler power.

4.4.3 Results

This subsection summarizes the results of the difference-frequency mixing experiment. Output idler wavelengths were generated from 1566.4 nm to 1652.5 nm by tuning the signal wavelength from 782.2 nm to 803.1 nm with a fixed pump wavelength at 530.9 nm. The power levels for the idler wavelengths generated from the DFM experiment are summarized in Tables 4.1 to 4.4 for various pump and signal input power levels. The pump power P_p is 80% of the actual power after the PBS from the krypton laser to take into account the 20% reflection loss from the coating of the front face of the

P_p (mW)	P_s (mW)	Measured P_i (μW)	Calculated P_i (μW)
156	37	0.905	1.092
124	37	0.707	0.868
92	37	0.510	0.644
60	37	0.329	0.420
28	37	0.164	0.196
156	24	0.559	0.708
156	11	0.280	0.325

Table 4.1: The measured and calculated output idler powers by difference-frequency mixing for various input power levels of the pump and signal with $\lambda_p = 530.9$ nm, $\lambda_s = 782.2$ nm and $\lambda_i = 1652.5$ nm.

P_p (mW)	P_s (mW)	Measured P_i (μW)	Calculated P_i (μW)
156	37	0.954	1.115
124	37	0.789	0.886
92	37	0.576	0.657
60	37	0.362	0.429
28	37	0.164	0.200
156	24	0.592	0.723
156	11	0.280	0.331

Table 4.2: The measured and calculated output idler powers by difference-frequency mixing for various input power levels of the pump and signal with $\lambda_p = 530.9$ nm, $\lambda_s = 786.6$ nm and $\lambda_i = 1633.2$ nm.

CTA crystal, while P_s is the actual power after the PBS from the Ti:sapphire laser. The measured output idler power ranges from 0.1 μW to 1.0 μW. Since the generated idler power is sufficiently small, the undepleted pump and signal assumptions used to derive Equation 3.8 is valid. To compare the expected output idler power calculated from Equation 3.8 and the observed data, we plotted the theoretical and measured values in Figures 4-11 to 4-15. From the tables and plots, we see that the generated idler powers are within $12 - 30\%$ of the calculated powers. Therefore, Equation 3.8 is a reasonably accurate expression to determine the output idler power.

The discrepancy of the calculated idler power and the measured power can be

P_p (mW)	P_s (mW)	Measured P_i (μW)	Calculated P_i (μW)
156	37	0.987	1.138
124	37	0.806	0.904
92	37	0.592	0.671
60	37	0.378	0.438
28	37	0.181	0.204
156	24	0.625	0.738
156	11	0.329	0.338

Table 4.3: The measured and calculated output idler powers by difference-frequency mixing for various input power levels of the pump and signal with $\lambda_p = 530.9$ nm, $\lambda_s = 791.1$ nm and $\lambda_i = 1614.1$ nm.

P_p (mW)	P_s (mW)	Measured P_i (μW)	Calculated P_i (μW)
156	37	0.938	1.161
124	37	0.724	0.923
92	37	0.526	0.685
60	37	0.362	0.447
28	37	0.181	0.208
156	24	0.576	0.753
156	11	0.296	0.345

Table 4.4: The measured and calculated output idler powers by difference-frequency mixing for various input power levels of the pump and signal with $\lambda_p = 530.9$ nm, $\lambda_s = 795.7$ nm and $\lambda_i = 1595.3$ nm.

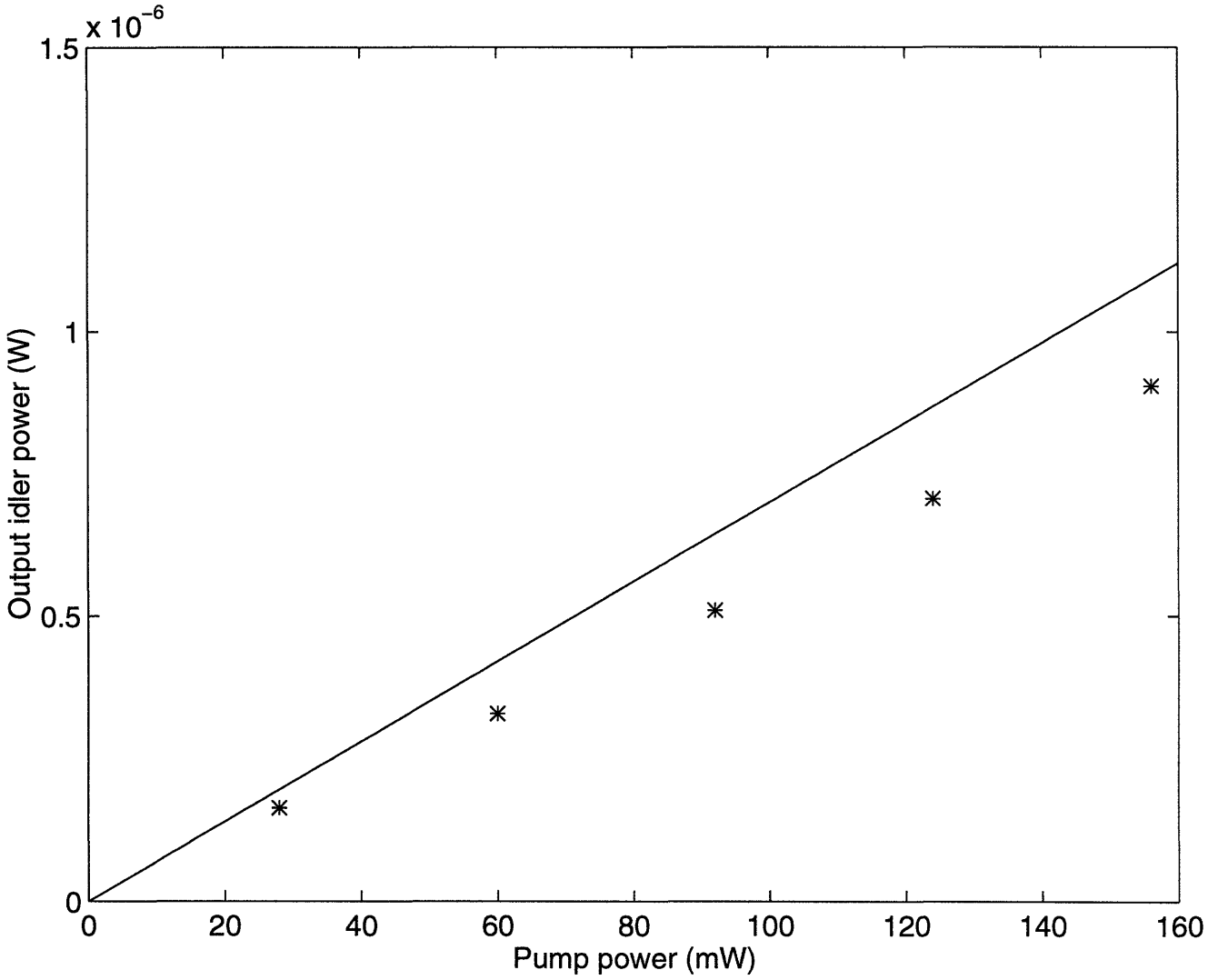

Figure 4-11: The generated output idler power as a function of the pump power at $\lambda_p = 530.9$ nm for a fixed signal power of 37 mW at $\lambda_s = 782.2$ nm. The solid line is the theoretical plot and the astericks represent the measured experimental data.

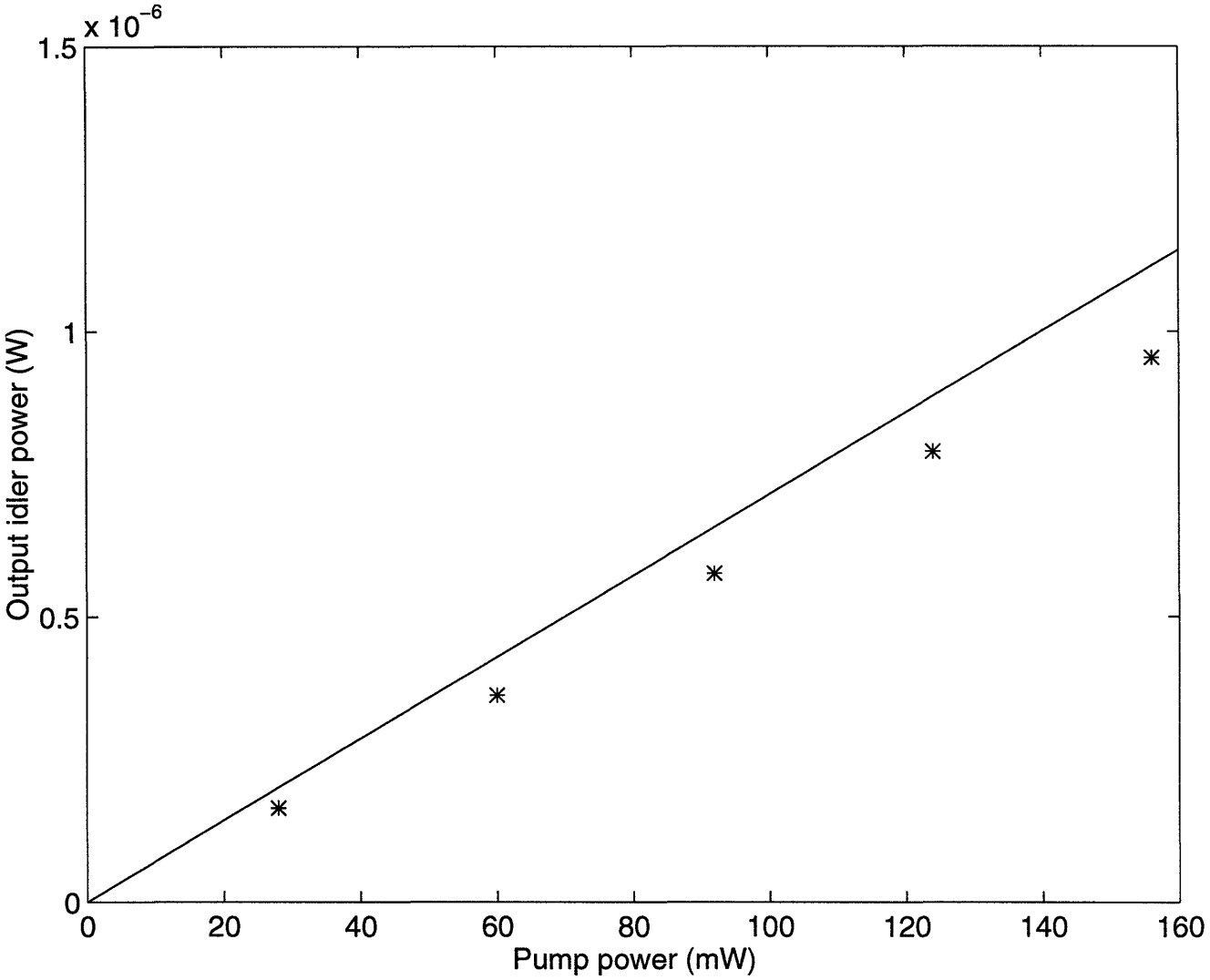

Figure 4-12: The generated output idler power as a function of the pump power at $\lambda_p = 530.9$ nm for a fixed signal power of 37 mW at $\lambda_s = 786.6$ nm. The solid line is the theoretical plot and the astericks represent the measured experimental data.

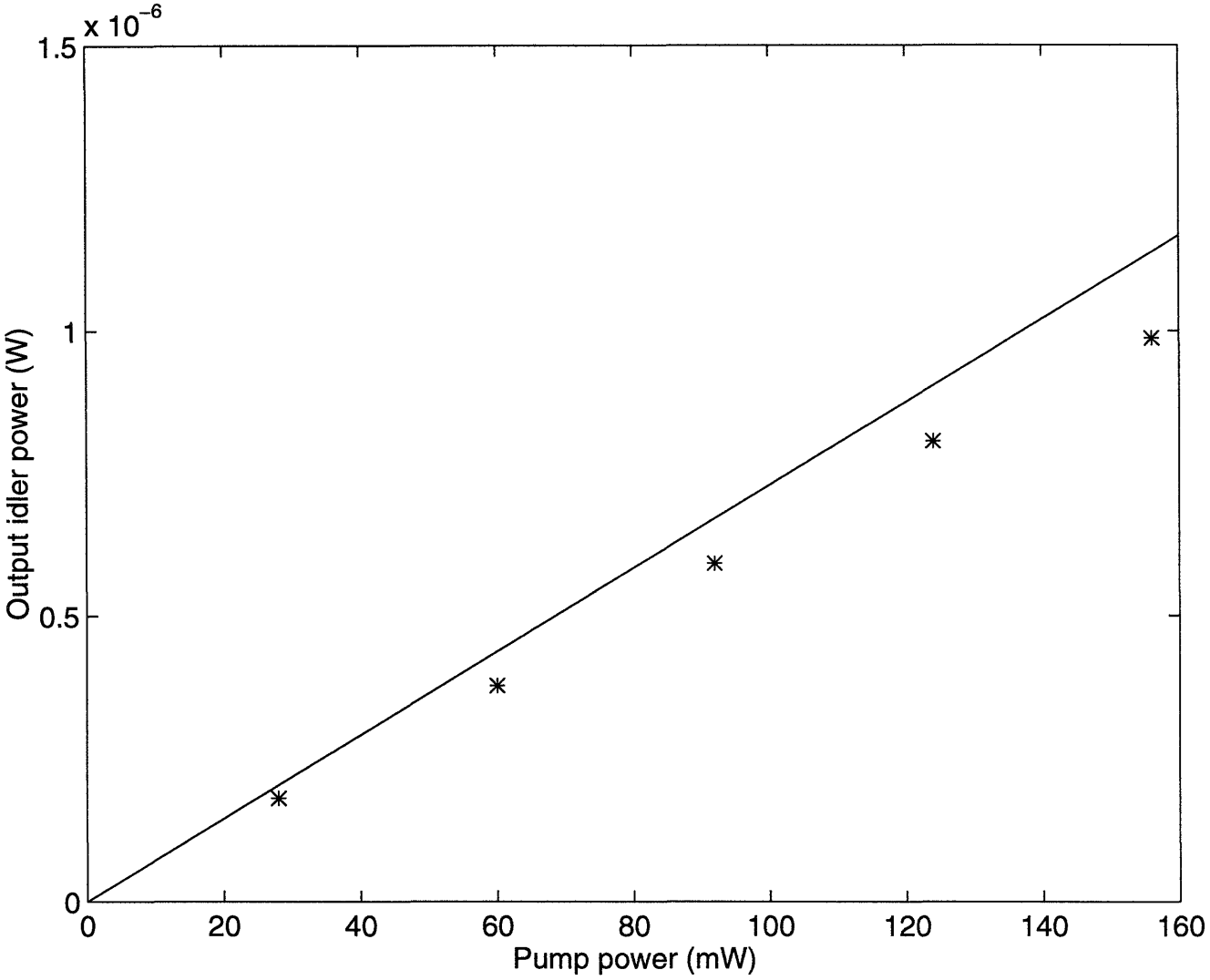

Figure 4-13: The generated output idler power as a function of the pump power at $\lambda_p = 530.9$ nm for a fixed signal power of 37 mW at $\lambda_s = 791.1$ nm. The solid line is the theoretical plot and the astericks represent the measured experimental data.

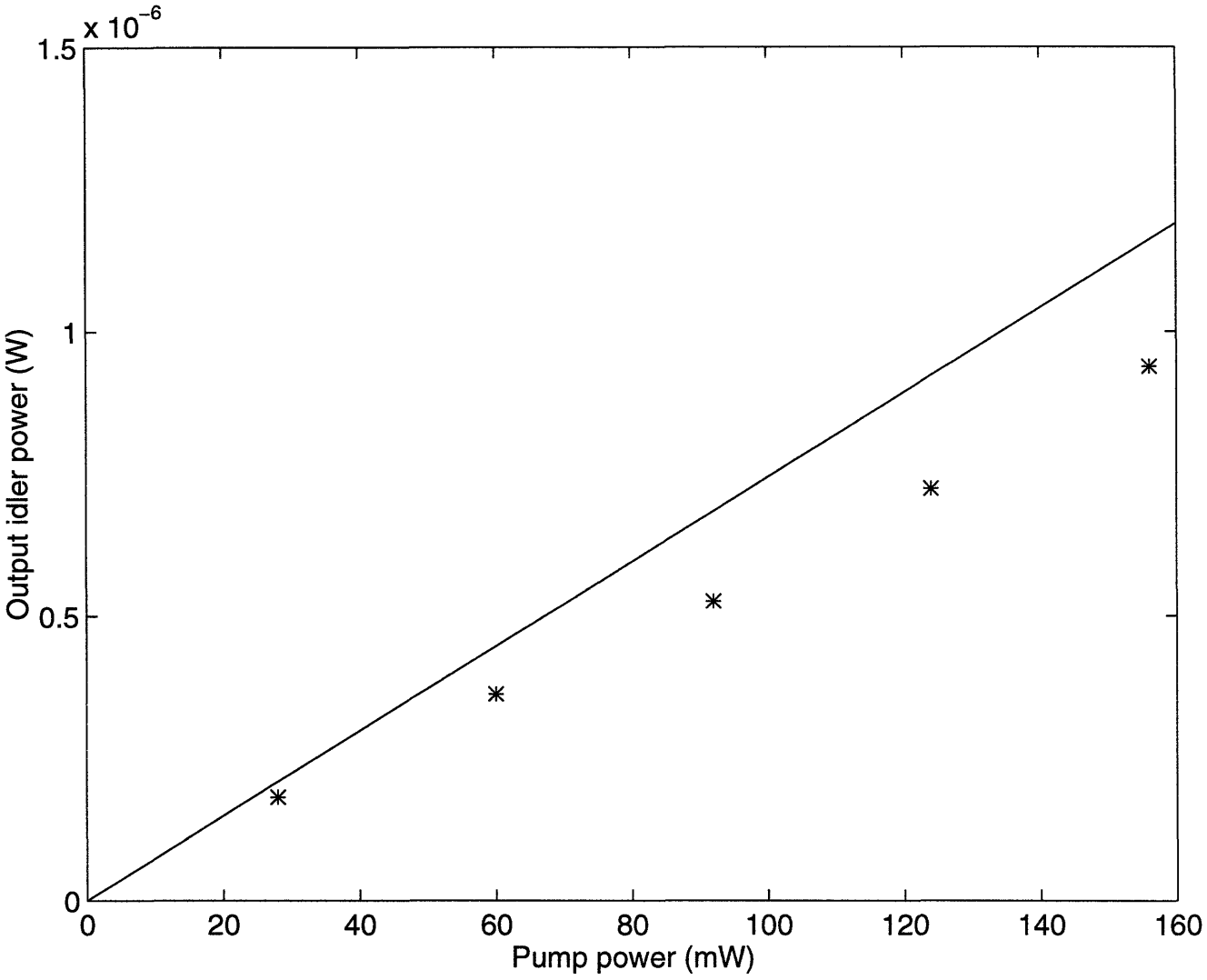

Figure 4-14: The generated output idler power as a function of the pump power at $\lambda_p = 530.9$ nm for a fixed signal power of 37 mW at $\lambda_s = 795.7$ nm. The solid line is the theoretical plot and the astericks represent the measured experimental data.

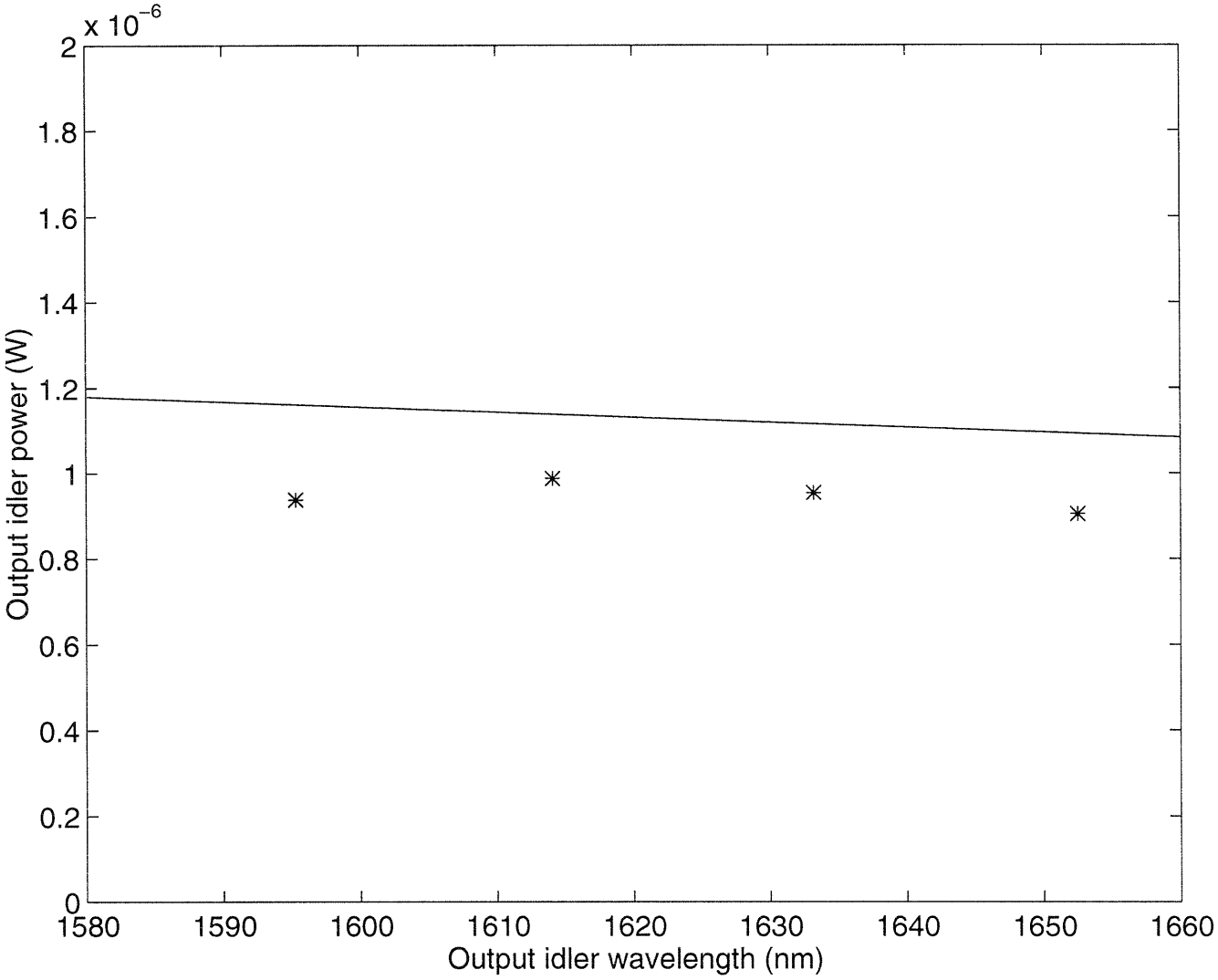

Figure 4-15: The generated output idler power as a function of the generated idler wavelength for a fixed pump and signal powers of 156 mW and 37 mW, respectively. The pump wavelength is $\lambda_p = 530.9$ nm. The solid line is the theoretical plot and the astericks represent the measured experimental data.

λ_s (nm)	λ_i (nm)	ϕ_{meas}	ϕ_{cal}
782.2	1652.5	41.03°	42.99°
785.2	1639.3	42.41°	44.75°
786.6	1633.2	42.88°	45.57°
787.4	1629.7	43.30°	46.03°
789.6	1620.4	44.30°	47.31°
791.1	1614.1	45.24°	48.18°
791.8	1611.2	45.50°	48.58°
795.7	1595.3	47.60°	50.85°
796.6	1591.7	48.18°	51.37°
803.1	1566.4	51.23°	55.19°

Table 4.5: The measured and calculated phase-matching angles for difference-frequency mixing with $\lambda_p = 530.9$ nm.

attributed to a number of factors. First, the pump and signal beams may not be perfectly mode-matched. Since the Ti:sapphire laser output is not completely circular due to the imperfect astigmatism compensation of the ring cavity, there may be incomplete spatial overlap of the pump and signal. Although not very likely, another source of discrepancy may be imperfect phase-matching in the θ and ϕ directions. In addition, since CTA is a new crystal, its actual nonlinear coefficients may be smaller than that determined by Cheng, et al., resulting in a smaller d_{eff} used to calculate the expected output idler power.

In addition to the output idler power, the internal phase-matching angle ϕ was also experimentally measured. The results are tabulated in Table 4.5 and shown in Figure 4-16. The measured internal phase-matching angle ϕ_{meas} was determined from the angle of incidence of the input beams. By using Snell's Law, we can determine the angle of incidence inside the crystal. Since the crystal is cut at $46.0° \pm 1°$, ϕ_{meas} can easily be found. The calculated phase-matching angle ϕ_{cal} is determined from the phase-matching condition presented in Section 3.3. A good agreement between the calculated and measured phase-matching angles is achieved over the entire tuning range. Therefore, the Sellmeier equations for CTA (Equations 4.1 to 4.3) are reasonably accurate. The tuning range of the idler wavelength for this CTA crystal is about 86 nm. This wavelength bandwidth is only limited by the crystal size and the tuning

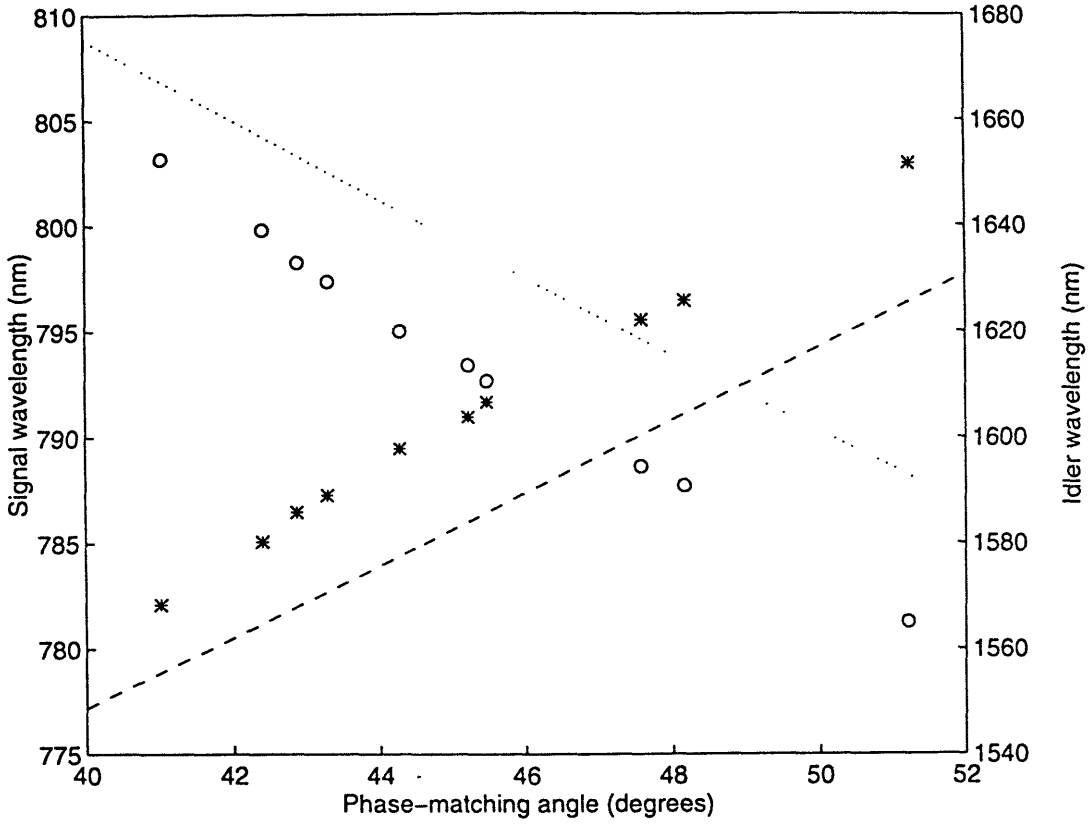

Figure 4-16: The experimental angle tuning curves for difference-frequency mixing in CTA. The calculated tuning curves, obtained from the Sellmeier equations, are shown as a dashed line for the signal wavelength and a dotted line for the idler wavelength. The pump wavelength is $\lambda_p = 530.9$ nm and the propagation direction is in the xy plane ($\theta = 90°$). The astericks and the circles represent the measured experimental data for the signal and idler wavelengths, respectively.

capability of the Ti:sapphire laser.

4.5 The RDFM Experiment

4.5.1 Experimental Setup

This subsection describes the setup for the CTA resonant difference-frequency mixing experiment. The experimental setup for RDFM is schematically shown in Figure 4-17. The RDFM cavity consisted of the CTA crystal symmetrically enclosed by a pair of spherical mirrors each with 25 cm radius of curvature and separated by 48 mm as shown in Figure 4-18. The two mirrors were each physically 7.75 mm in diameter and 4 mm thick. The front mirror served as the input coupler for the pump and was coated for high transmission at the pump wavelength, and high reflection at the signal and idler wavelengths. The back mirror served as the input coupler for the signal beam as well as the output coupler for the idler beam and was coated to highly reflect the pump and partially transmit the signal and idler. The power reflectivities of the cavity mirrors were directly measured to be 1.4% at λ_p, 99.7% at λ_s, and 99.7% at λ_i for the front mirror, and 99.0% at λ_p, 99.2% at λ_s, and 99.5% at λ_i for the back mirror. Finesse measurements were also performed at $\lambda_s = 790.0$ nm and $\lambda_i = 1.53$ μm. For the empty cavity case, the finesse was 570 for the signal and 625 for the idler. With the CTA crystal in the cavity, the finesse was 200 for the signal.

To make fine adjustments of the cavity length, the back mirror was mounted on a piezoelectric transducer (PZT). The back mirror and the PZT were held by a flexure mount (Newport, Model MFM-100) to allow fine adjustments of the back mirror position for alignment of the RDFM cavity. A ramp generator (Burleigh, Model RC-43) and a function generator (Wavetek, Model 182) were used for applying a high-voltage triangular waveform with equal rise and fall times across the PZT. As the voltage increased, the back mirror moved closer to the front mirror. When the voltage decreased after the peak, the back mirror returned to its initial position and repeated the same motion. The tuning rate of the PZT was about 1 nm/V.

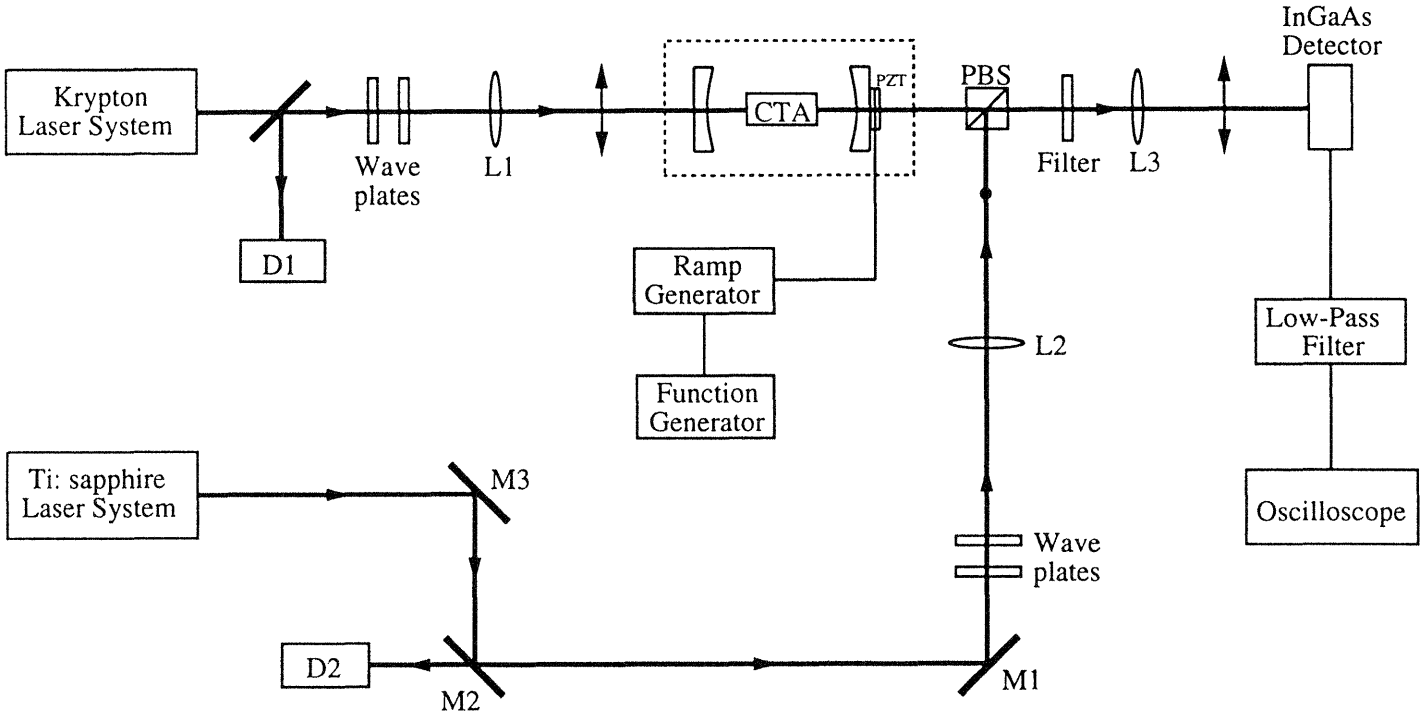

Figure 4-17: The experimental setup for resonant difference-frequency mixing in CTA.

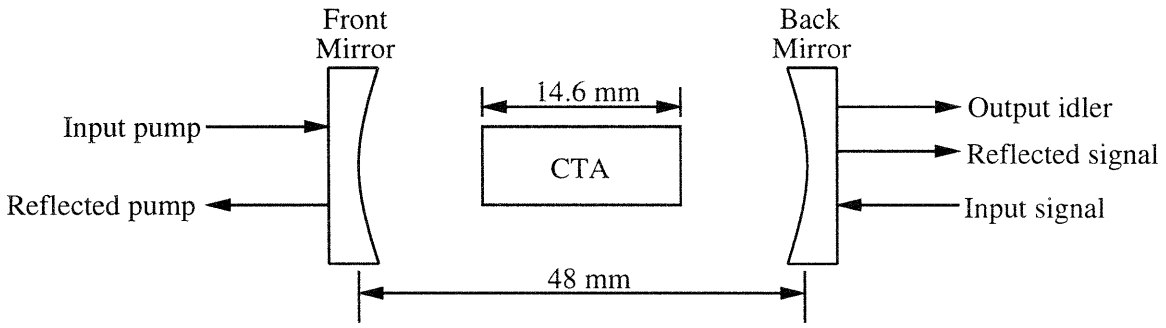

Figure 4-18: The cavity configuration for resonant difference-frequency mixing in CTA.

Since the back mirror has a higher transmission for the signal wavelength, it served as the input coupler for the input signal. Therefore, the pump and signal beams entered at opposite ends of the RDFM cavity. The pump beam was focused using a plano-convex lens (L1) with 25 cm focal length and entered the cavity through the front mirror. The signal was focused with a 20 cm focal length plano-convex lens (L2) through the back mirror. The lenses, mounted on xyz translation stages, were positioned such that the focus was at the center of the crystal and mode-matched to the cavity with $b = 3.65$ cm inside the crystal. With this confocal parameter, the beam waists of the three waves at the center of the CTA crystal were 40 μm for the pump, 49 μm for the signal, and 71 μm for the idler. The polarizing beam splitter (PBS) was used to allow the input signal beam to enter the RDFM cavity and also to separate the output idler and the reflected signal for detection. A high-pass filter was used to transmit the idler and block the pump and signal beams. The photodetectors, D1 and D2, were used to detect the reflected pump and signal beams, respectively. The output idler beam was focused by a bi-convex lens (L3) with 25.4 cm focal length into an InGaAs photodetector with feedback resistance of 100kΩ. The DC voltage output of the InGaAs photodetector then passed through a low-pass filter (Stanford Research Systems, Model SR650) to reduce noise and provide signal gain.

4.5.2 Experimental Procedures

This subsection describes the procedures for the alignment and optimization of the resonant difference-frequency mixing process to generate the maximum output idler power at $\lambda_i = 1618.7$ nm for input wavelengths of $\lambda_p = 530.9$ nm and $\lambda_s = 790.0$ nm. With the RDFM cavity mirrors and the mode-matching lenses (L1 and L2) taken out, the pump and signal beams were adjusted such that they passed straight through the CTA crystal. When L1 and L2 were placed back in, the pump and signal beams should propagate through the crystal more or less parallel to each of the four side faces of the crystal. Next, the orientation of the CTA crystal was adjusted so that the input pump beam was reflected directly back from the front end of the crystal. Then we rotated the crystal in the ϕ direction such that the angle of incidence was approximately 3° at the front end of the crystal. This angle was extrapolated from the DFM experiment for $\lambda_s = 790.0$ nm.

As an initial check of the correct placement of the mode-matching lens, we adjusted L1 and L2 in the y direction to locate the foci of the two input beams in air. Then we adjusted the lenses in the z direction to position the foci at the center of the crystal. Since there were material imperfections with the CTA crystal, we needed to adjust L1 in the x and y directions to find an area where the transmitted beam through the crystal was clear (no scattering or distortions). Unlike the difference-frequency mixing experiment, finding a good spot is very critical to obtaining the maximum generated output idler power for RDFM since the losses can add up due to the multiple-pass nature of the cavity.

Next we aligned the front mirror of the RDFM cavity such that the reflected pump beam from the mirror overlapped the incident pump beam. For proper mode-matching, the spot size of the reflected pump beam should be about the same as that of the input beam. It was convenient to compare the spot sizes at L1. If the reflected spot size was smaller than the input spot size, moving L1 towards the RDFM cavity (z direction) increased the reflected spot size. Conversely, L1 was moved away from the cavity if the reflected spot size was larger. Finally, we aligned the back mirror

to reflect the input pump beam directly back. Again the spot sizes of the input and reflected beams should be similar.

The fine alignment of the RDFM cavity to the pump beam consisted of observing the reflected pump at D1 while the cavity was scanned for one free spectral range of the pump resonance. To perform this scan, the PZT was driven with a 300 V peak-to-peak triangular wave at 60 Hz. Since the cavity was low-finesse for the pump, the detected signal was a sinusoidal waveform. The flexure mount holding the back mirror was then adjusted to obtain the largest peak-to-peak signal. Small adjustments of L1 was also done to improve the alignment. Since the pump beam was now well-aligned, we used the transmitted pump beam through the RDFM cavity and the polarizing beamsplitter to align L3 to couple the maximum light onto the InGaAs photodetector.

With the RDFM cavity now well-aligned for the pump beam, the next major step was to align the signal beam to be collinear with the pump beam through the CTA crystal. Before we perform this alignment, the signal beam should first be mode-matched to the RDFM cavity. Like the pump beam, we compared the spot sizes of the input and reflected signal beam at L2. Then L2 was appropriately adjusted as described earlier for L1 such that the spot size of the reflected beam from the two cavity mirrors was comparable to that of the input signal beam.

The alignment of the signal beam was best accomplished by adjusting the input signal beam to spatially overlap the transmitted pump beam through the RDFM cavity. If the signal beam was collinear with the transmitted pump beam at every point between M3 and the back mirror, then the pump and signal beams should copropagate through the RDFM cavity. With L2 taken out, we first adjusted M3 so that the signal beam overlapped the pump beam at M2. Since the two spot sizes were not the same, various points between M2 and M3 were also used for better overlap. M2 was then adjusted to overlap the signal and pump at M1. Again various points between M1 and M2 were used for better alignment. Finally M1 was adjusted to obtain overlap at points between M1 and the back mirror of the cavity.

Next, we placed L2 back in and adjusted it in the x and y directions to spatially overlap the signal beam with the pump beam at points between L2 and the cavity

back mirror. Now we can perform the same adjustments on M1, M2 and M3 as discussed earlier to overlap the signal beam to the pump beam. Since both the pump and signal beams were well mode-matched, the spot sizes of the two beams should be comparable at all points between M3 and L2. Due to the initial alignment performed earlier, only small adjustments of the mirrors was necessary.

In order for the InGaAs photodetector to detect the output idler resonances, we needed to change the spacing between the cavity mirrors at least over a range of 800 nm. By scanning the RDFM cavity, we were also able to observe the reflected signal resonances at D2 for fine alignment of the signal beam. For a scan of 800 nm, we obtained two free spectral ranges of the signal beam or three resonances. If the signal beam was not well-aligned, we should see lower order modes (smaller resonances) in addition to the three main resonances. We then adjusted M1, M2 and L2 to collapse the lower-order modes to the main resonances. During this alignment, output idler resonances was generated as long as the pump and signal beams remained collinear.

When the signal beam was well-aligned, we were able to easily generate idler resonances by finely tuning the crystal in the ϕ direction and finely adjusting the back mirror using the flexure mount. After these adjustments were made, it was necessary to readjust L2, M1 and M2 to realign the signal beam. Therefore, optimizing the output idler power was quite difficult and time-consuming since iterative adjustments of L1, L2, M1, M2, the flexure mount and the crystal position were all required to generate the maximum possible output idler power. The optimization was further complicated by the instability of the generated idler resonances due to the large absorption of the CTA crystal at the pump and signal wavelength.

4.5.3 Results

This subsection summarizes the results of the resonant difference-frequency mixing experiment. A typical plot of the generated output idler power by resonant difference-frequency mixing as the PZT is scanned is shown in Figure 4-19. The ramp voltage driving the PZT, the reflected pump and the reflected signal are also included in the graph. The maximum generated output idler powers for various input pump and

signal power levels are summarized in Table 4.6 and shown in Figures 4-20 to 4-22. The generated idler powers range from 10 μW to 100 μW.

The theoretical values for the generated output idler power are calculated from Equation 3.39 with $d_{\text{eff}} = 2.69$ pm/V, $\bar{h}_m(B,\xi) = 0.15$, $\chi^2 = 6.30 \times 10^{-23}$ s, $\kappa_p = 0.883$, $\kappa_s = 0.0155$, $\kappa_i = 0.04$, $t_p^2 = 0.986$, $t_s^2 = 0.008$, and $t_i^2 = 0.005$. However, since the back mirror of the RDFM cavity is highly reflective for the pump wavelength, the pump in effect makes a double pass through the CTA crystal, increasing the generated idler power by a factor of between two and four.[11] Due to the 20% reflection of the pump at the faces of the CTA crystal, this enhancement factor is reduced by 82%. For an enhancement factor of 2.46, we find that the measured idler powers are about a factor of three smaller than the theoretical values (see Table 4.6). This large discrepancy of the measured and calculated idler powers may be accounted for by reflection phase shifts at the RDFM cavity mirrors, imperfect mode matching, and the uncertainty of the enhancement factor due to the double pass of the pump. However, the discrepancy is most likely due to the uncertainty in the cavity losses. Specifically, the cavity mirror reflectivities and the CTA crystal absorption at the idler wavelength were determined using a 1.53 μm diode laser. Since the generated idler wavelength is around 1.6 μm, the total cavity loss κ_i may actually be a factor of two larger. In this case, the measured idler powers are within several percent of the calculated idler powers.

A major problem with the RDFM experiment was that the output idler does not stay stable for very long. The main reason for this instability is the poor optical quality of the CTA crystal. When the idler power is generated, the RDFM cavity is well-aligned for both the pump and signal beams, and a large amount of power propagates through the crystal. Since the CTA crystal exhibits a relatively large absorption at the three interacting wavelengths, the crystal physically heats up, changing the principal refractive indices of the crystal and the optical cavity length. Therefore, after a certain brief amount of time, the cavity goes out of resonance. Since the cavity is off resonance, the power through the crystal decreases, and the crystal begins to cool down. After a while, the crystal may cool to the original temperature,

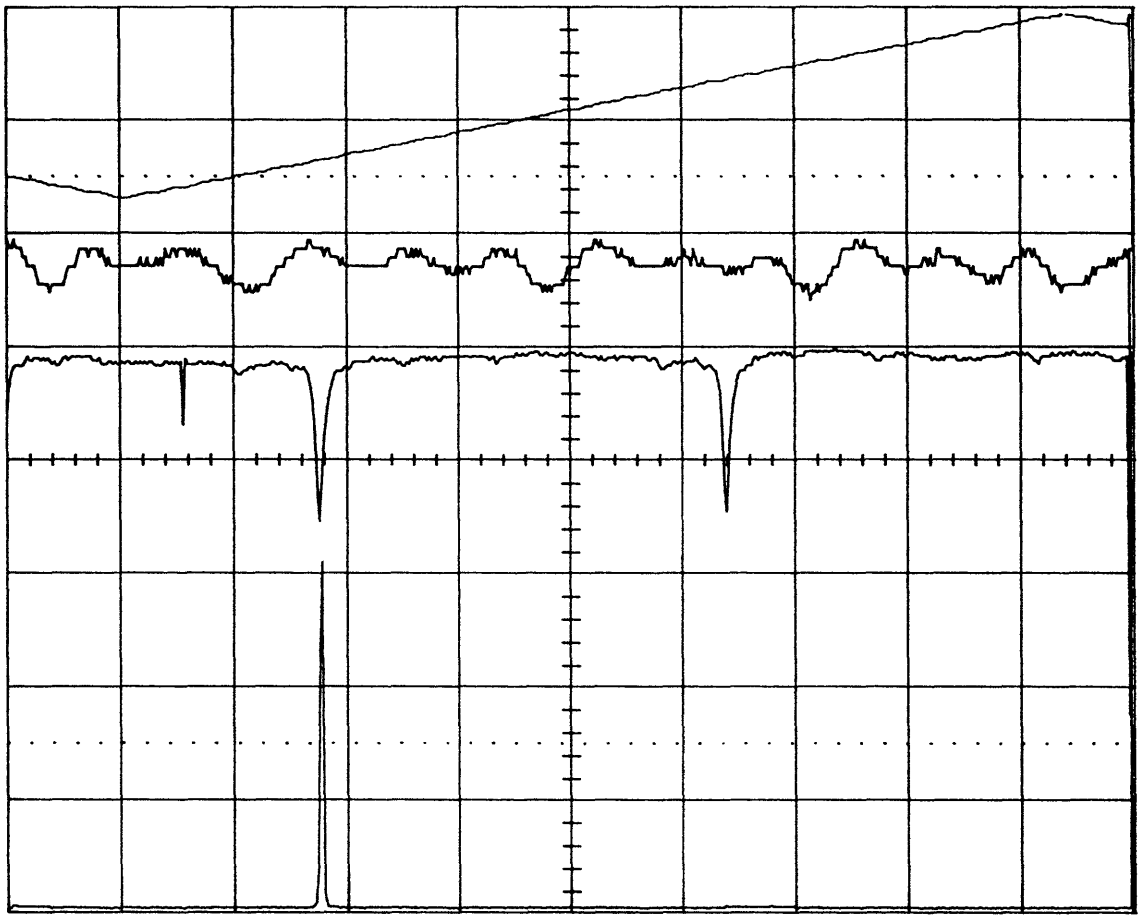

Figure 4-19: Plot of the detected power of the three interacting wavelengths as the RDFM cavity length is scanned. The four plots from top to bottom represent the voltage scan, reflected pump, reflected signal and output idler.

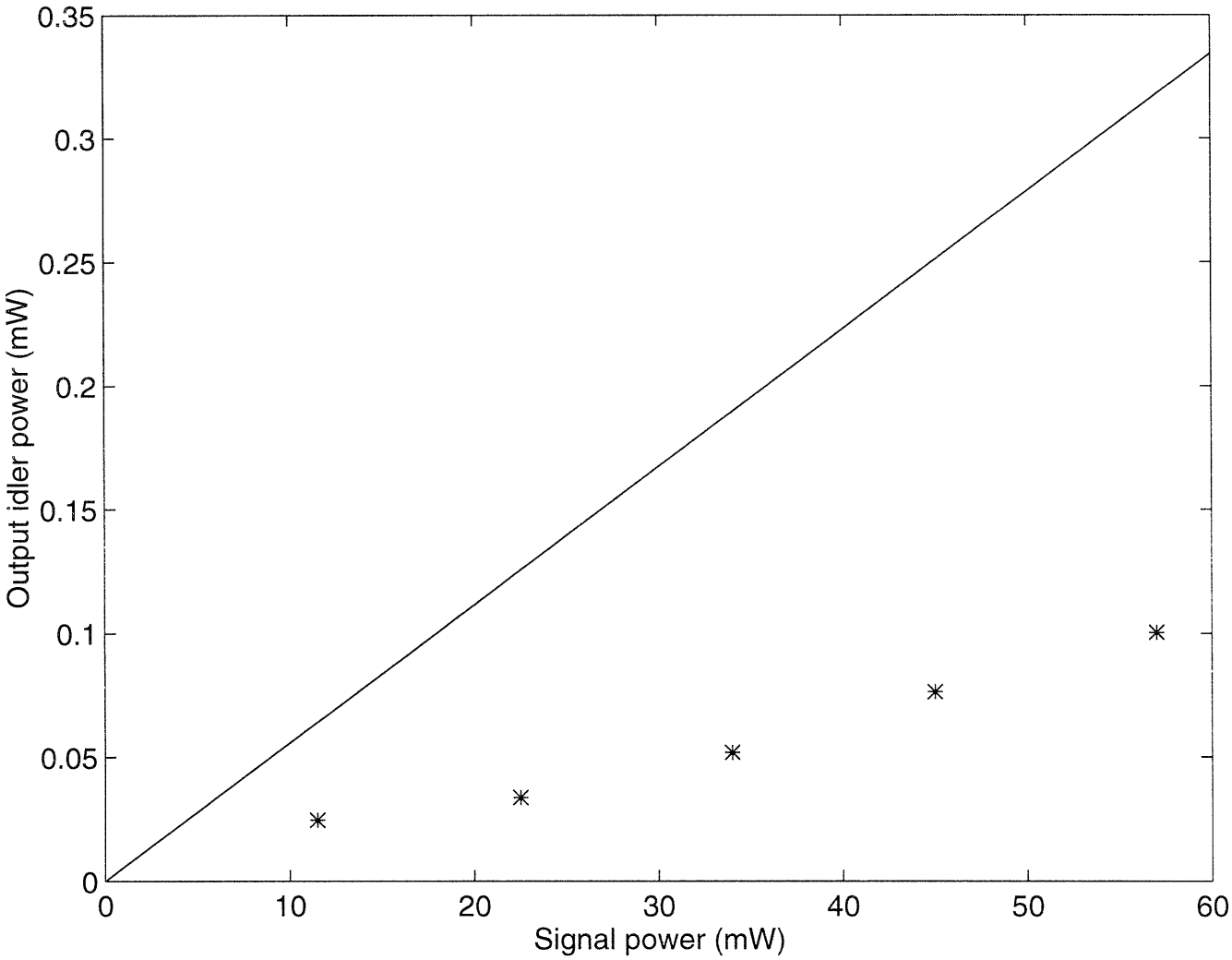

Figure 4-20: The output idler power versus the input signal power at $\lambda_s = 790.0$ nm for a fixed pump power of 230 mW at $\lambda_p = 530.9$ nm. The solid line is the calculated plot and the astericks represent the measured experimental data.

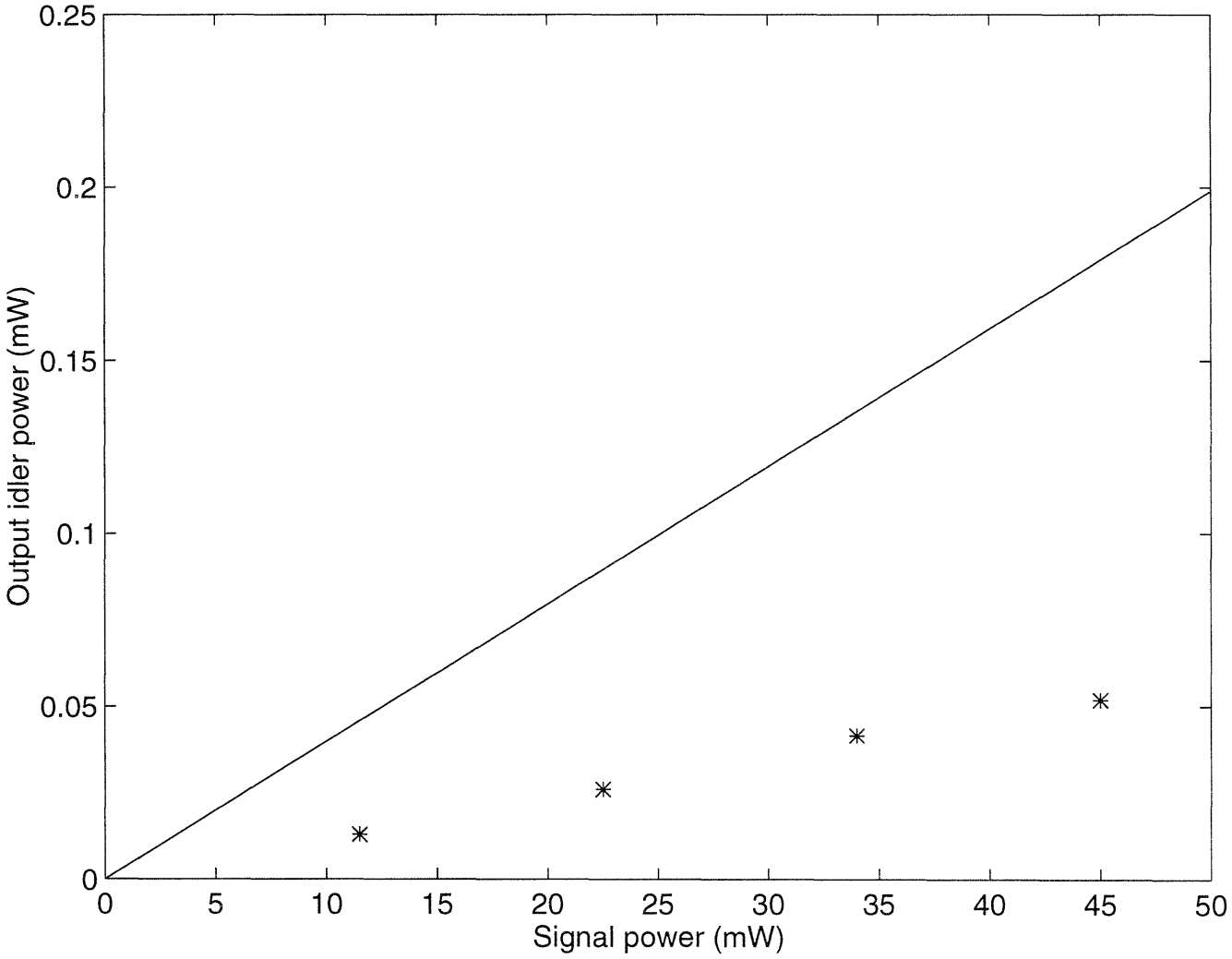

Figure 4-21: The output idler power versus the input signal power at $\lambda_s = 790.0$ nm for a fixed pump power of 170 mW at $\lambda_p = 530.9$ nm. The solid line is the calculated plot and the astericks represent the measured experimental data.

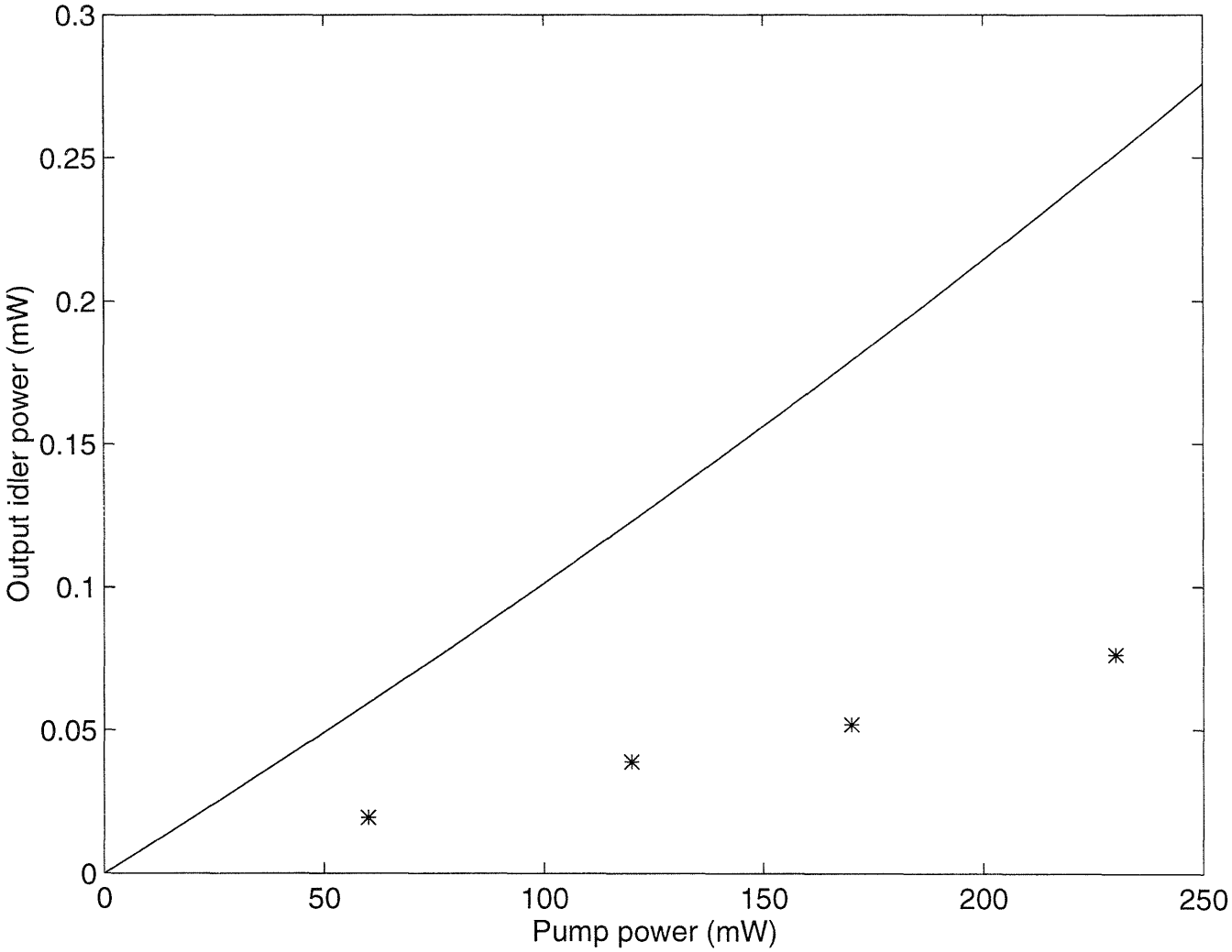

Figure 4-22: The output idler power versus the pump power at $\lambda_p = 530.9$ nm for a fixed signal power of 45 mW at $\lambda_s = 790.0$ nm. The solid line is the calculated plot and the astericks represent the measured experimental data.

P_p (mW)	P_s (mW)	Measured P_i (μW)	Calculated P_i (μW)
230	57	100.39	317.72
230	45	76.45	250.83
230	34	51.83	189.52
230	22.5	33.69	125.42
230	11.5	24.62	64.10
170	45	51.83	179.04
170	34	41.46	135.28
170	22.5	25.92	89.52
170	11.5	12.96	45.76
120	45	38.87	122.82
60	45	19.44	59.37

Table 4.6: The measured and calculated output idler powers by resonant difference-frequency mixing for various input power levels of the pump and signal with $\lambda_p =$ 530.9 nm, $\lambda_s = 790.0$ nm, and $\lambda_i = 1618.7$ nm.

and if the alignment has not been changed, the idler will be generated again. The crystal then begins to heat up again and the same process occurs.

The instability of the idler resonances may also be compounded by the refraction of the interacting beams at various points along the CTA crystal. This beam refraction is caused by the inhomogeneity in the CTA material probably due to the nonuniform growth process of the CTA crystal. Therefore, when the three interacting beams propagate through the crystal, they experience a propagation walk-off due to imperfect CTA crystal quality. This beam walk-off contributes to the instability of the generated idler resonances and may account for the relatively large cavity losses determined by the finesse measurements.

Chapter 5

Conclusion

5.1 Summary

Difference-frequency mixing in CTA was demonstrated to provide tunable infrared outputs in the range between 1.57 and 1.65 μm using a krypton-ion laser and a Ti:sapphire laser as the input sources. The measured angle phase-matching tuning curve determined by the DFM experiment was in good agreement with that predicted from the Sellmeier equations for CTA. The generated output idler power ranged from 0.1 μW to 1 μW for pump powers of $28 - 156$ mW and signal powers of $11 - 37$ mW. These measured output idler powers for the DFM experiment were in good agreement with the calculated values. Resonant difference-frequency mixing in CTA was also demonstrated for an output idler wavelength of $\lambda_i = 1618.7$ nm. The maximum generated output power was 100.39 μW for a pump power of 230 mW and signal power of 57 mW. The measured output idler powers for the RDFM experiment were a factor of three smaller than the theoretical values.

5.2 Further Research

Due to the large absorption characteristics of the CTA crystal, optical parametric oscillation could not be achieved. If the absorption is reduced to 0.5%, then the OPO threshold calculated from Equation 3.43 is about 50 mW, which can easily be

obtained from a krypton laser. With improvements in the CTA crystal quality, the CTA optical parametric amplifier/oscillator may potentially be realized and become the tunable source of choice for many application in the future.

We can also investigate other nonlinear crystals such as lithium triborate (LBO) as an alternative to CTA. From the Sellmeier equations, we see that tunable outputs at 1.6 μm is possible by Type I phase-matching in LBO at $\theta = 90^{\circ}$ and $\phi = 11.6^{\circ}$ using the same krypton and Ti:sapphire lasers as inputs. By heating this crystal to 148°C, we can operate at $\theta = 90^{\circ}$ and $\phi = 0^{\circ}$ to eliminate Poynting vector walk-off. In this case, the threshold of 40 mW is low enough for OPO operation.

Since the output idler was very unstable, it would also be helpful to investigate techniques to stabilize the idler resonances. One method is to stabilize the crystal temperature by using a thermo-electric (TE) cooler and standard locking techniques to stabilize the output idler. To obtain stability for the idler frequency, the two input lasers should also be frequency stabilized.

Appendix A

Effective Area of Gaussian Beams

The radial variation in the transverse electric field of a Gaussian beam in the near field of the fundamental mode is given by

$$\mathbf{E}(r) = \mathbf{E}_0 e^{-r^2/w_0^2}. \tag{A.1}$$

The power generated by the Gaussian beam can be calculated by evaluating the following integral:

$$\begin{aligned} P_0 &= \frac{nc\epsilon_0}{2} \int |\mathbf{E}(r)|^2 r dr d\phi \\ &= \frac{nc\epsilon_0}{2} \int_0^{2\pi} \int_0^{\infty} |\mathbf{E}_0|^2 r e^{-2r^2/w_0^2} dr d\phi \\ &= \frac{nc\epsilon_0}{2} |\mathbf{E}_0|^2 \int_0^{2\pi} \frac{w_0^2}{4} d\phi \\ &= I_0 \left(\frac{\pi w_0^2}{2} \right). \end{aligned} \tag{A.2}$$

Therefore the effective Gaussian beam area is

$$\mathcal{A} = \frac{\pi w_0^2}{2}. \tag{A.3}$$

Appendix B

The Effective Nonlinear Coefficient

The second-order nonlinear polarization produced by the various field components in a lossless medium can be written in matrix form as[12]

$$\begin{bmatrix} P_x \\ P_y \\ P_z \end{bmatrix} = \epsilon_0 \begin{bmatrix} d_{11} & d_{12} & d_{13} & d_{14} & d_{15} & d_{16} \\ d_{21} & d_{22} & d_{23} & d_{24} & d_{25} & d_{26} \\ d_{31} & d_{32} & d_{33} & d_{34} & d_{35} & d_{36} \end{bmatrix} \begin{bmatrix} E_{1,x}E_{2,x} \\ E_{1,y}E_{2,y} \\ E_{1,z}E_{2,z} \\ E_{1,y}E_{2,z} + E_{1,z}E_{2,y} \\ E_{1,x}E_{2,z} + E_{1,z}E_{2,x} \\ E_{1,x}E_{2,y} + E_{1,y}E_{2,x} \end{bmatrix}.$$

Since CTA belongs in the $mm2$ orthorhombic symmetry class, its d_{ijk} matrix is given by

$$d_{ijk} = \begin{bmatrix} 0 & 0 & 0 & 0 & d_{15} & 0 \\ 0 & 0 & 0 & d_{24} & 0 & 0 \\ d_{31} & d_{32} & d_{33} & 0 & 0 & 0 \end{bmatrix}.$$

A linearly polarized wave in an biaxial crystal can be expressed as a superposition of the ordinary and extraordinary waves. For Type II phase-matching ($o+e \rightarrow o$) in the xy plane ($\theta = 90°$), the electric field components of the two orthogonally polarized

waves along the xyz crystallographic axes, where z is the main optic axis, are[12]

$$\mathbf{E}_1 = \mathbf{E}^o = \begin{bmatrix} E_x^o \\ E_y^o \\ E_z^o \end{bmatrix} = \begin{bmatrix} -E^o \sin\phi \\ E^o \cos\phi \\ 0 \end{bmatrix}$$

and

$$\mathbf{E}_2 = \mathbf{E}^e = \begin{bmatrix} E_x^e \\ E_y^e \\ E_z^e \end{bmatrix} = \begin{bmatrix} 0 \\ 0 \\ -E^e \end{bmatrix},$$

where the superscripts o and e represents the ordinary and extraordinary waves, respectively. Therefore, the polarization components are

$$\begin{aligned} P_x &= \epsilon_0 d_{15}(E_x^o E_z^e + E_z^o E_x^e) \\ &= \epsilon_0 d_{15} \sin\phi E^o E^e, \qquad \text{(B.1)} \\ P_y &= \epsilon_0 d_{24}(E_y^o E_z^e + E_z^o E_y^e) \\ &= -\epsilon_0 d_{24} \cos\phi E^o E^e, \qquad \text{(B.2)} \\ P_z &= \epsilon_0(d_{31} E_x^o E_x^e + d_{32} E_y^o E_y^e + d_{33} E_z^o E_z^e) \\ &= 0. \qquad \text{(B.3)} \end{aligned}$$

These components are then used to calculate the total second-order nonlinear polarization:

$$\begin{aligned} P &= P^o + P^e \\ &= -P_x \sin\phi + P_y \cos\phi - P_z \\ &= -\epsilon_0(d_{15} \sin^2\phi + d_{24} \cos^2\phi) E^o E^e. \qquad \text{(B.4)} \end{aligned}$$

Therefore, the effective second-order nonlinear coefficient is

$$d_{\text{eff}} = -(d_{15} \sin^2\phi + d_{24} \cos^2\phi). \qquad \text{(B.5)}$$

Bibliography

[1] J. A. Armstrong, N. Bloembergen, J. Ducuing, and P. S. Pershan. "Interactions between light waves in a nonlinear dielectric." *Physical Review*, Vol. 127, No. 6, pp. 1918-39, 1962.

[2] K. Asaumi. "Second-harmonic power of $KTiOPO_4$ with double refraction." *Applied Physics B*, Vol. 54, pp. 265-70, 1992.

[3] R. A. Baumgartner and R. L. Byer. "Optical parametric amplification." *IEEE Journal of Quantum Electronics*, Vol. QE-15, No. 6, pp. 432-44, 1979.

[4] G. D. Boyd and A. Ashkin. "Theory of parametric oscillator threshold with single-mode optical masers and observation of amplification in $LiNbO_3$." *Physical Review*, Vol. 146, No. 1, pp. 187-98, 1966.

[5] G. D. Boyd and D. A. Kleinman. "Parametric interaction of focused Gaussian light beams." *Journal of Applied Physics*, Vol. 39, No. 8, pp. 3597-639, 1968.

[6] F. Brehat and B. Wyncke. "Calculation of double-refraction walk-off angle along the phase-matching directions in non-linear biaxial crystals." *Journal of Physics B*, Vol. 22, pp. 1891-9, 1989.

[7] R. L. Byer. "Optical parametric oscillators." in *Treatise in Quantum Electronics*, H. Rabin and C. L. Tang, eds., pp. 587-702, 1975.

[8] P. Canarelli, Z. Benko, R. Curl, and F. K. Tittel. "Continuous-wave infrared laser spectrometer based on difference frequency generation in $AgGaS_2$ for high-

resolution spectroscopy." *Journal of the Optical Society of America B*, Vol. 9, No. 2, pp. 197-202, 1992.

[9] L. K. Cheng, L. T. Cheng, F. C. Zumsteg, J. D. Bierlein, and J. Galperin. "Development of the nonlinear optical crystal $CsTiOAsO_4$: Crystal growth and characterization." *Journal of Crystal Growth*, Vol. 132, pp. 289-96, 1993.

[10] L. T. Cheng, L. K. Cheng, J. D. Bierlein, and F. C. Zumsteg. "Nonlinear optical and electro-optical properties of single crystal $CsTiOAsO_4$." *Applied Physics Letters*, Vol. 63, No. 19, pp. 2618-20, 1993.

[11] T. Debuisschert, A. Sizmann, E. Giacobino, and C. Fabre. "Type-II continuous-wave optical parametric oscillators: oscillation and frequency-tuning characteristics." *Journal of the Optical Society of America B*, Vol. 10, No. 9, pp. 1668-80, 1993.

[12] V. G. Dmitriev, G. G. Gurzadyan, and D. N. Nikogosyan. *Handbook of Nonlinear Optical Crystals*, 1991.

[13] M. M. Fejer. "Nonlinear optical frequency conversion." *Physics Today*, pp. 25-33, May 1994.

[14] S. Guha and J. Falk. "The effects of focusing in the three-frequency parametric upconverter." *Journal of Applied Physics*, Vol. 51, No. 1, pp. 50-60, 1980.

[15] S. E. Harris. "Tunable optical parametric oscillators." *Proceedings of the IEEE*, Vol. 57, pp. 2096-113, 1969.

[16] A. H. Heilscher, C. E. Miller, D. C. Bayard, U. Simon, K. P. Smolka, R. F. Curl, and F. K. Tittel. "Optimization of a midinfrared high-resolution difference-frequency laser spectrometer." *Journal of the Optical Society of America B*, Vol. 9, No. 11, pp. 1962-7, 1992.

[17] T. F. Johnston and W. Proffitt. "Design and performance of a broad-band optical diode to enforce one-direction traveling-wave operation of a ring laser." *IEEE Journal of Quantum Electronics*, Vol. QE-16, No. 4, pp. 483-8, 1980.

[18] M. Kaschke and C. Koch. "Calculation of nonlinear optical polarization and phase matching in biaxial crystals." *Applied Physics B*, Vol. 49, pp. 419-23, 1989.

[19] H. W. Kogelnik, E. P. Ippen, A. Dienes, and C. V. Shank. "Astigmatically compensated cavities for cw dye lasers." *IEEE Journal of Quantum Electronics*, Vol. QE-8, No. 3, pp. 373-9, 1972.

[20] H. Kogelnik and T. Li. "Laser beams and resonators." *Applied Optics*, Vol. 5, No. 10, pp. 1550-67, 1966.

[21] J. A. Kong, *Electromagnetic Wave Theory*, 1986.

[22] P. F. Moulton. "Spectroscopic and laser characteristics of Ti:Al_2O_3." *Journal of the Optical Society of America B*, Vol. 3, No. 1, pp. 125-32, 1986.

[23] A. S. Pine. "Doppler-limited molecular spectroscopy by difference-frequency mixing." *Journal of the Optical Society of America*, Vol. 64, No. 12, pp. 1683-90, 1974.

[24] K. C. Rustagi and P. K. Gupta. "Effect of Gaussian intensity profiles on difference-frequency generation." *Optics Communications*, Vol. 33, pp.103-7, 1980.

[25] P. A. Schulz. "Single-frequency Ti:Al_2O_3 ring laser." *IEEE Journal of Quantum Electronics*, Vol. 24, No. 6, pp. 1039-44, 1988.

[26] K. Sun. "Classical and quantized fields in optical parametric interactions." PhD Thesis, Massachusetts Institute of Technology, September 1993.

[27] W. Wang and M. Ohtsu. "Frequency-tunable sum- and difference-frequency generation by using two diode lasers in a KTP crystal." *Optics Communications*, Vol. 102, pp. 304-8, 1993.

[28] B. Wyncke and F. Brehat. "Calculation of the effective second-order non-linear coefficients along the phase matching directions in acentric orthorhombic biaxial crystals." *Journal of Physics B*, Vol. 22, pp. 363-76, 1989.

[29] J. Q. Yao and T. S. Fahlen. "Calculation of optimum phase match parameters for the biaxial crystal $KTiOPO_4$." *Journal of Applied Physics*, Vol. 55, No. 1, pp. 65-8, 1984.

[30] B. Wellegehausen, D. Friede, H. Vogt, and S. Shahdin. "Generation of tunable cw infrared radiation by difference frequency mixing." *Applied Physics*, Vol. 11, pp. 363-70, 1976.

[31] S. Zhu. "Birefringent filter with tilted optic axis for tuning dye lasers: theory and design." *Applied Optics*, Vol. 29, No. 3, pp. 410-5, 1990.

[32] W. Q. Zhang. "Optical parametric generation for biaxial crystal." *Optics Communications*, Vol. 105, pp. 226-32, 1994.